Theoretical and Applied Fracture Mechanics 141 (2026) 105069

Contents lists available at ScienceDirect

Theoretical and Applied Fracture Mechanics

journal homepage: www.elsevier.com/locate/tafmec

Crack path under non-proportional fatigue loading — Evaluating tests with existing crack growth direction criteria

Sjoerd T. Hengeveld [a,b,*], Davide Leonetti [b], H.H. (Bert) Snijder [b], Johan Maljaars [a,b]

[a] Reliable Structures, TNO, Molengraaffsingel 8, Delft, 2629 JD, The Netherlands
[b] Structural Engineering and Design, Eindhoven University of Technology, De Zaale 1, Eindhoven, 5612 AZ, The Netherlands

ARTICLE INFO

Dataset link: https://zenodo.org/records/15807377

Keywords:
Fatigue crack growth direction
Non-proportional load
Finite element analyses
Experimental evaluation

ABSTRACT

Proper descriptions of the fatigue crack growth rate and direction are crucial for determining the residual fatigue life of metallic structures. In non-proportional multi-axial loading, the prediction of the fatigue crack growth direction is not trivial. This study evaluates the effect of different state-of-the-art crack growth direction criteria on the predicted crack paths by comparing the results with experiments with non-proportional load done by others. The results are compared in terms of predicted angles at different experimental crack lengths and cumulative predicted crack path. Based on this study, it is concluded that none of the studied criteria based on linear elastic fracture mechanics is able to accurately predict the crack growth direction in non-proportional loading for the general case. The mismatch of some cases studied is so large that these criteria cannot be used in crack growth path prediction for an arbitrary, non-proportional load case.

1. Introduction

Fatigue is one of the most important failure mechanisms for metallic structures under fluctuating loads. The fatigue life of a structure can be divided into three phases: (1) Initiation of a crack from the uncracked structure (2) Stable crack growth from the initiated crack and (3) final fracture of the remaining ligament [1]. In the stable crack growth regime, determining the remaining fatigue life requires an accurate description of the fatigue crack growth rate (FCGR) and FCGD. Assuming linear elastic fracture mechanics (LEFM) and ignoring the effect of the microstructure, the crack path for physically long cracks under applied uniaxial loading is perpendicular to the direction of the maximum principal stress. However, multi-axial loading is present in most practical cases, such as notched geometries. Within multi-axial loading, distinction is made between proportional and non-proportional loading. Proportional loading is characterised by a constant orientation of principal stress during a load cycle [2]. The crack driving force in Mode-I and Mode-II mixed-mode (multi-axial) loading is often assessed by combining the respective SIFs, K_I and K_{II}, into an equivalent SIF, K_{eq}. Numerous expressions for K_{eq} exist in literature, often determined from experimental data, some have a preference for K_I, and some have a preference for K_{II} [3–5]. Several researchers studied fatigue crack growth in proportional loading, focusing on Mode-I and Mode-II load [6] or Mode-I and Mode-III load [7]. Two FCGDs compete in proportional load, namely, perpendicular to the maximum principal stress, and aligned with the maximum shear stress [8]. However, the first direction usually dominates [9].

Determining the FCGD and FCGR in non-proportional mixed-mode load appears non-trivial. Non-proportional load conditions arise in several practical applications, such as coil springs in automotive [10] and in rolling contact fatigue (RCF) in wheel–rail systems [11,12]. Most experiments with non-proportional load aim at studying or predicting FCGR [13–16] whereas a minority of studies aim at the FCGD [17,18]. Hereafter, a compilation is given of a few experimental lessons learned on FCGD. A FCGD close to the plane perpendicular to the maximum principal stress (range) is referred to as Mode-I dominated, and a FCGD in a plane aligned with the maximum shear stress (range) is referred to as Mode-II (or Mode-III) dominated, see Fig. 1(a). The effect of cyclic Mode-II load with a constant Mode-I load on FCGD was studied in [19,20]. Both studies showed that compression at the crack tip, leads to contact between the crack faces. This resulted into a lower FCGR and a more Mode-II dominated FCGD as compared to experiments with a zero or positive Mode-I component. Bold [20] showed that experiments with a static positive Mode-I component resulted in small, coplanar, Mode-II crack growth (0.05 mm to 0.1 mm) before deviating to a Mode-I dominated FCGD, see Fig. 1(b). Similarly, Bonniot et al. [21,22], investigated the FCGR in R260 rail steel subjected

* Corresponding author at: Structural Engineering and Design, Eindhoven University of Technology, De Zaale 1, Eindhoven, 5612 AZ, The Netherlands.
E-mail address: s.t.hengeveld@tue.nl (S.T. Hengeveld).

https://doi.org/10.1016/j.tafmec.2025.105069
Received 31 March 2025; Received in revised form 18 June 2025; Accepted 30 June 2025
Available online 10 September 2025

Nomenclature

Symbols

$\mathbf{a}^{\pm}$	Trial vectorial crack increment used in vector crack tip displacement criterion
$\mathbf{a}$	Vectorial crack increment used in vector crack tip displacement criterion
a	Crack length
$a_i^{\bullet}$	Crack length with identifier i, for experiment $\bullet$
a_n	Notch length
$A_{\bullet,\bullet}$	Coefficients in the relation between K and K^r
c_{II}	Mode-II coefficient in Hourlier-Pineau criterion
$\hat{\mathbf{e}}_{\theta}$	Unit vector in direction of fatigue crack growth direction
E, E'	Regular and Effective Young's modulus
f^+, f^-	Trial functions limiting crack growth in vector crack tip displacement criterion
F_x, F_x	Applied load in x-direction and y-direction in cruciform specimen
K_I, K_{II}	Mode I and Mode-II stress intensity factor
K_{eq}	Equivalent stress intensity factor
$k_{I,F_x}, k_{I,F_y}, k_{II,F_x}, k_{II,F_y}$	Mode I and Mode II stress intensity factor components for unit load cases applied in the x- and y-directions
K_I^r, K_{II}^r	Mode-I and Mode-II stress intensity factor for an infinitely small crack increment around the crack-tip
p	Reference point used in finite element simulation
R	Stress ratio
r	Distance to crack-tip
R_p	Plastic zone radius
s_i	Crack extensions steps i
t	Time within a load cycle
t_{in}, t_{out}	Thickness cruciform specimen (in crack growth region, in clamping region)
$u^{\pm}, v^{\pm}$	Horizontal and vertical displacement of point on a distance r from the crack tip
u_x, u_y	Horizontal and vertical displacement components in finite element model
u_{px}, u_{py}	Horizontal and vertical displacement components of reference points in finite element model
W	Normalized plastic zone radius
w_c	Walker mean stress correction coefficient
w_{2d}	Width of area used finite element simulations
x, y	Axis in global coordinate system
x', y'	Axis in coordinate system aligned with crack tip
$\mathbf{x_g}$	Crack path in Cartesian coordinates
Y_{σ}, Y_{τ}	Geometrical correction factors for Mode-I and Mode-II
Δa	Crack increment
$\Delta K_{I,w_c}$	Stress intensity factor range including Walker mean stress correction
$\delta_I, \delta_{II}, \delta$	Crack displacement used in (Mode-I, Mode-II, total)
θ_c	Fatigue crack growth direction angle in crack-tip coordinate system
θ_g	Fatigue crack growth direction angle in global coordinate system
$\Delta\lambda$	Biaxiality ratio of the stress intensity factor ranges, $\Delta K_{II}/\Delta K_I$
λ	Biaxiality ratio between stress intensity factor components, K_{II}/K_I
ν	Poisson's ratio
σ	Nominal stress perpendicular to crack front
σ_1	Maximum principal stress
$\sigma_r, \sigma_{\theta}, \tau_{r\theta}$	Stress components in a cylindrical coordinate system with the origin at the crack-tip
σ_{ys}	Von Mises equivalent stress
τ	Nominal shear stress along the crack front
ϕ_F	Phase shift between F_x and F_y in a cruciform specimen
ϕ_K	Phase shift between K_I and K_{II}
ψ	Parameter governing locking in vector crack tip displacement criterion

Subscripts (multiple used)

$_{exp}$	Experiment
$_{max}$	Maximum during a cycle
$_{mean}$	Mean during a cycle
$_{min}$	Minimum during a cycle

Operators

$\Delta\bullet$	Range of variable $\bullet$
$\langle\bullet\rangle$	Macaulay brackets
$\overline{\langle\bullet\rangle}$	Variation of Macaulay brackets
$\tilde{\bullet}$	Fluctuation of displacement used in vector crack tip displacement

Acronyms

DOF	Degree of freedom
FCGD	Fatigue crack growth direction
FCGR	Fatigue crack growth rate
FE	Finite element
HP	Hourlier-Pineau
LEFM	Linear elastic fracture mechanics
MERR	Maximum energy release rate
MPZR	Minimum plastic zone radius
MSSR	Maximum shear stress range
MTS	Maximum tangential stress
PICC	Plasticity induced crack closure
RCF	Rolling contact fatigue
RICC	Roughness induced crack closure
SEN(B)	Single edge notched specimen in bending
SIF	Stress intensity factor
VCCT	Virtual crack closure technique
VCTD	Vector Crack Tip Displacement

to non-proportional load. They showed that a cyclic Mode-II load in combination with a compressive cyclic Mode-I load led to longer Mode-II crack growth compared to experiments with cyclic Mode-II load combined with a tensile cyclic Mode-I load. The latter experiments

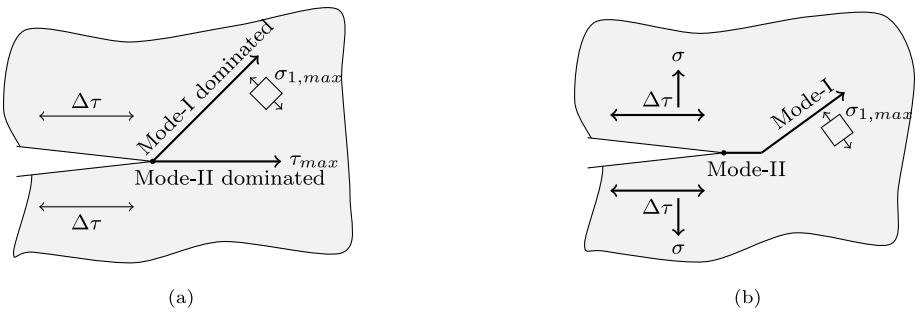

Fig. 1. (a) Example of Mode-I and Mode-II dominated crack growth in a pure Mode-II load scenario. (b) Example of Mode-II crack growth before deviating to a Mode-I dominated crack.

showed almost a completely Mode-I dominated FCGD. The FCGD also depends on the relative magnitude of the Mode-I and Mode-II load components. Otsuka et al. [23] conducted experiments on aluminium alloys 2017-T3 and 7075-T6 and showed that a Mode-II dominated FCGD is observed if $\Delta K_{II}/\Delta K_I > 1.6$, provided ΔK_{II} is sufficiently large to generate crack growth. Crack growth in Mode-I direction was observed if these conditions were not met. All tests were conducted with positive Mode-I components. Zerres and Vormwald [24] concluded that the FCGR in non-proportional mixed-mode loading depends on the mode-mixity, i.e. the ratio between K_{II} and K_I, material properties affecting cyclic plasticity and crack closure, applied load, and the specimen geometry. As the FCGD is related to the FCGR, the authors of the current paper assume that the same influence parameters are important for the FCGD. Doquet et al. [25] conducted experiments on tubular specimens made of maraging steel, subjected to different non-proportional load schemes. Evaluation of these experiments using elastic–plastic FE models again showed that there is competition between Mode-I dominated and Mode-II FCGD. Most experiments showed straight crack growth, aligning with predictions for those cases. However, the experiments with a non-zero FCGD were not predicted well. Bonniot et al. [21,22] experimentally investigated the effect of contact between the crack faces on Mode-I/II crack growth using thin-walled tubular specimens. In several experiments they observed crack branching, in which the crack splits in a co-planar crack in the Mode-II dominated FCGD and a crack in the Mode-I dominated FCGD. Due to these branches, they observed crack face shielding between the crack with a Mode-I dominated FCGD and the crack with a Mode-II dominated FCGD, effectively reducing the Mode-II SIF, depending on the mode-mixity.

Several criteria have been proposed to determine the FCGD, all originally developed for proportional load, such as the MTS criterion, [26,27], the maximum energy release rate (MERR) [28], the maximum shear stress range (MSSR) criterion [17,29] and the VCTD criterion. The latter is extended in [17] to be used in non-proportional load situations. These criteria will be elaborated in Section 3.1. Highsmith [30] evaluated some of these FCGD criteria, showing that FCGD is not solely defined by the Mode-I range and the Mode-II range but that there is influence of the Mode-I and Mode-II mean SIF, which is material dependent. He proposes a variation of the MTS criterion combined with a Walker mean stress correction [31] for a better agreement with experimental data compared to the original MTS. Amato et al. [32] used the MTS criterion to predict crack growth in proportional and non-proportional load. They evaluated single-edge notched specimens made of high-strength steel (34CrNiMo6) subjected to cyclic tension and cyclic torsion load [7]. They simulated crack growth using 3D FE models to obtain SIFs and an incremental MTS criterion to evaluate the FCGD. Simulations with fully reversed cyclic axial stress ($R_\sigma = -1$) showed good agreement with the corresponding experimental results. However, simulations with a stress ratio $R_\sigma = 0$ showed a large deviation with the experiments. Infante-García et al. [18] used the extended FE method to determine the SIFs in biaxial non-proportional load conditions, using several variations of the MTS criterion to predict the FCGD and crack path. They showed that the variations studied had a large influence on the predicted FCGD. Moreover, it is demonstrated that, depending on the criterion used, a reasonable approximation of the FCGD at a predefined crack length does not necessarily imply an accurate prediction of the entire crack path. Doquet et al. [25], made a distinction between Mode-I and Mode-II dominated crack growth by using two different damage criteria, allowing to calculate the theoretical fatigue life of each direction separately and assuming the crack grows in the direction of highest crack growth rate.

Infante-García et al. [18] and Amato et al. [32] did not include the effect of contact between the crack faces in their simulations. From a mechanical point of view, contact could influence the effective SIF and thereby potentially the FCGD. Therefore, distinction is made here between the nominal SIF, which is the SIF related to the applied load and ignoring the effects of contact and plasticity, and the effective SIF, which is the part of the SIF beyond opening of the crack, which contributes to fatigue crack growth [33]. Some mechanisms that influence this effectiveness are given here. First, plasticity induced crack closure (PICC) [33] occurs due to development of plasticity around the crack-tip, reducing the effective Mode-I SIF. Several models are developed to estimate the effect of PICC, such as the NASGRO model [34]. Secondly, roughness induced crack closure (RICC) reduces the Mode-I SIF, in case the roughness is of the same order of magnitude as the crack tip opening displacement [35]. In the near-threshold regime, where this displacement is small, RICC often results in zig-zag fracture paths [20,25,31,36]. Depending on the closure level, this zig-zag pattern can lead to a crack-tip sliding displacement, generating an effective Mode-II SIF even in case of a nominal pure Mode-I load [37]. In pure Mode-II load this zig-zag pattern can result in an additional effective ΔK_I [37]. Finally, friction between the crack faces reduces the sliding displacement and thereby reduces ΔK_{II}. In general, all three described effects, the zig-zag pattern, friction, and crack-closure, are present in mixed-mode load in load cases where crack face contact may happen. This leads to a complex interaction between Mode-I and Mode-II. Several models are developed to describe this interaction [38–40]. These models provide a qualitative description of the interaction between these effects. However, quantifying this interaction appears too complex to-date. The development of PICC depends on the crack tip constraint, which is a function of the crack shape, geometry and material properties. Hence there is a difference between plane strain and plane stress situations. Capturing PICC requires non-linear FE models. None of the above-mentioned non-proportional FCGD criteria account for PICC and RICC. Pommier et al. [41–44] developed a FCGR framework accounting for the effects of plasticity. The deformation and translation of the plastic zone around the crack-tip is described in their model throughout the complete load history, making a distinction between the elastic and plastic SIF components. The model is based on elastic–plastic FE models and can also be used to predict FCGR in variable amplitude loading [41,44]. Their framework shows potential for FCGD prediction assuming that the FCGR is indeed proportional to the development of plasticity. However, extending Pommier's framework to predict the

Table 1
FCGD criteria considered within this research.

Method	Ref:
Maximum tangential stress (MTS)[a]	[26]
Maximum shear stress range (MSSR)	[17]
Vector Crack Tip Displacement (VCTD)[b]	[17]
Hourlier-Pineau (HP)	[46]
Minimum plastic zone radius (MPZR)[c]	[47]

[a] Augmented with a Walker mean stress correction factor [30].
[b] In addition, to the original implementation, the authors of the current study propose a variant.
[c] The criterion is developed for proportional load. The authors of the current study implemented it for non-proportional load.

FCGD requires a relation between the development of plasticity and the FCGD, which is currently not available.

Floros et al. [17] evaluated the FCGD using the VCTD criterion, based on experimental data from the literature. Both linear elastic and elastic–plastic material behaviour were considered. They concluded that the VCTD applied with linear elasticity agrees better with the experimental results. Dahlin and Olsson [45] used the MTS criterion and a maximum tangential stress range criterion in combination with elastic–plastic FE models to predict the FCGD. They demonstrated that using elastic–plastic material behaviour provided more accurate FCGD predictions compared to using linear elastic material behaviour. However, there appears to be no criterion to differentiate between the MTS and the maximum tangential stress range criterion. The studies show that using elastic–plastic material behaviour does not necessarily result in improved FCGD predictions compared to linear elastic material behaviour. This is possibly due to the fact that the criteria are originally developed for linear elasticity.

Up to the authors' knowledge, a universal criterion for predicting the FCGD for non-proportional mixed-mode load does not exists. The goal of the current study is to evaluate existing FCGD criteria by comparing the predicted crack paths to experimental crack paths from non-proportional mixed-mode experiments described in the literature. Crack growth simulations using linear elastic FE models of the experiments are made to facilitate this evaluation. The FCGD criteria are compared at different instances at specific experimental crack paths, predicting solely an extension direction. In addition, they are applied in crack growth simulations in which the cumulative crack path is predicted. Table 1 lists the criteria considered in this study. These criteria are selected as these are the most used criteria in the literature. The MERR is not included in this comparison as it is strongly related to the Hourlier-Pineau (HP) criterion. All criteria are based on LEFM. Therefore, experiments are selected with an almost completely positive K_I through the entire cycle, in order to limit crack closure effects. The reasoning is that any valid model should at least be able to predict this simple case. Linear elastic material behaviour is used in this research as all considered criteria in this research are all developed for or can be applied without modification to linear elastic material. This also reduces numerical complexity in crack growth simulations.

2. Applied experiments and FCGD criteria

This section gives the descriptions of the selected FCGD criteria and of the selected non-proportional mixed-mode fatigue experiments used to evaluate the criteria. In general, K_I and K_{II} for a crack length a are related to the nominal stress field by:

$$K_I(t) = \sigma(t)\, Y_\sigma(a)\sqrt{\pi a}, \quad K_{II}(t) = \tau(t)\, Y_\tau(a)\sqrt{\pi a} \tag{1}$$

in which σ is the stress perpendicular to the crack front and τ is the nominal shear stress along the crack front, both quantities defined for the uncracked condition. Y_σ and Y_τ are geometric correction factors. The stress field in the vicinity of the crack front can be approximated by the first order Westergaard stress field solutions [48] in terms of a polar coordinate system defined at the crack tip, see Fig. 2(a):

$$\begin{bmatrix}\sigma_r(\theta_c,r,t)\\ \sigma_\theta(\theta_c,r,t)\\ \tau_{r\theta}(\theta_c,r,t)\end{bmatrix} = \frac{1}{4\sqrt{2\pi r}}\begin{bmatrix}5\cos\frac{\theta_c}{2}-\cos\frac{3\theta_c}{2}, & -5\sin\frac{\theta_c}{2}+3\sin\frac{3\theta_c}{2}\\ 3\cos\frac{\theta_c}{2}+\cos\frac{3\theta_c}{2}, & -3\sin\frac{\theta_c}{2}-3\sin\frac{3\theta_c}{2}\\ \sin\frac{\theta_c}{2}+\sin\frac{3\theta_c}{2}, & \cos\frac{\theta_c}{2}+3\cos\frac{3\theta_c}{2}\end{bmatrix}\begin{bmatrix}K_I(t)\\ K_{II}(t)\end{bmatrix} \tag{2}$$

in which σ_r, σ_θ and $\tau_{r\theta}$ are the stress components in cylindrical coordinates and $t \in (0,1)$ is the normalised time during a cycle. A cycle in non-proportional load is defined as the smallest, fully repetitive load sequence, see Fig. 3. All criteria are written in terms of SIFs of an infinitely small crack increment from the crack tip [48], see Fig. 2(b):

$$\begin{bmatrix}K_I^r(\theta_c,t)\\ K_{II}^r(\theta_c,t)\end{bmatrix} = \sqrt{2\pi r}\begin{bmatrix}\sigma_\theta(\theta_c,r,t)\\ \tau_{r\theta}(\theta_c,r,t)\end{bmatrix} = \begin{bmatrix}A_{I,I}(\theta_c), & A_{I,II}(\theta_c)\\ A_{II,I}(\theta_c), & A_{II,II}(\theta_c)\end{bmatrix}\begin{bmatrix}K_I(t)\\ K_{II}(t)\end{bmatrix} \tag{3}$$

with coefficients:

$$\begin{aligned}A_{I,I}(\theta_c) &= \frac{1}{4}\left(3\cos\frac{\theta_c}{2}+\cos\frac{3\theta_c}{2}\right)\\ A_{I,II}(\theta_c) &= \frac{1}{4}\left(-3\sin\frac{\theta_c}{2}-3\sin\frac{3\theta_c}{2}\right)\\ A_{II,I}(\theta_c) &= \frac{1}{4}\left(\sin\frac{\theta_c}{2}+\sin\frac{3\theta_c}{2}\right)\\ A_{II,II}(\theta_c) &= \frac{1}{4}\left(\cos\frac{\theta_c}{2}+3\cos\frac{3\theta_c}{2}\right)\end{aligned} \tag{4}$$

Most FCGD criteria do not depend on the absolute load level, but on the mode-mixity, described by the biaxiality ratio λ:

$$\lambda(t,\theta_c) = \frac{K_{II}^r(t,\theta_c)}{K_I^r(t,\theta_c)} \tag{5}$$

A load sequence is defined as proportional if λ is constant. Similarly, the biaxiality range is defined as:

$$\Delta\lambda = \frac{\Delta K_{II}}{\Delta K_I} \tag{6}$$

The remainder of this section elaborates different experiments and criteria using these concepts.

2.1. Experimental data

The experimental data considered in this study are obtained from literature. Experiments were selected based on the specimen type and the applied load. The research focuses on cruciform specimens, e.g Fig. 4, as these allow for complete decoupling between Mode-I and Mode-II load, and the specimens can be modelled in a 2D FE analysis. The K_I component should be positive through the entire load cycle and crack path, to minimize crack closure effects. Another prerequisite is that the experimental crack path is known. Experiments showing significant crack branching are omitted as it is assumed that interaction between the cracks cannot be captured by any of the FCGD criteria. Two experimental sources are chosen based on these selection criteria. Both experimental setups are such that the direction of the far-field principal stresses is constant through the test and therefore the far-field stresses remain proportional. However, the local stresses near the crack tip, which drive the FCGD, do not remain proportional. Due to the similitude principle, the local stress field describes the SIF evolution independent of the far field stresses.

2.1.1. Biaxial load with phase shifts

Wolf et al. [14,15] measured the FCGR in high alloy austenitic stainless steel (X5CrMnNi16-7-7) cruciform specimens, focusing on the effect of load phase shift on the crack growth rate. Fig. 4(a) shows a

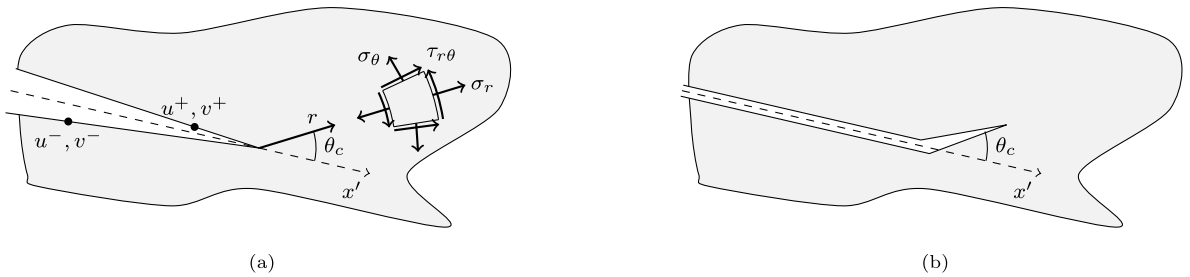

Fig. 2. Crack tip and coordinate system for an infinitely small, rotated crack increment. (a) Polar coordinate system and corresponding stress components (b) infinitely small crack increment from the crack-tip.

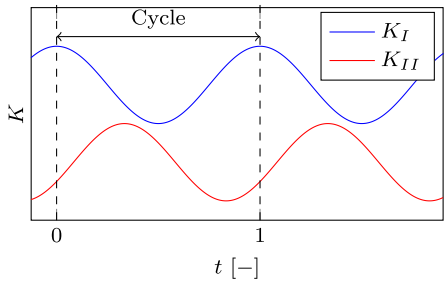

Fig. 3. Example load sequence with indication of cycle.

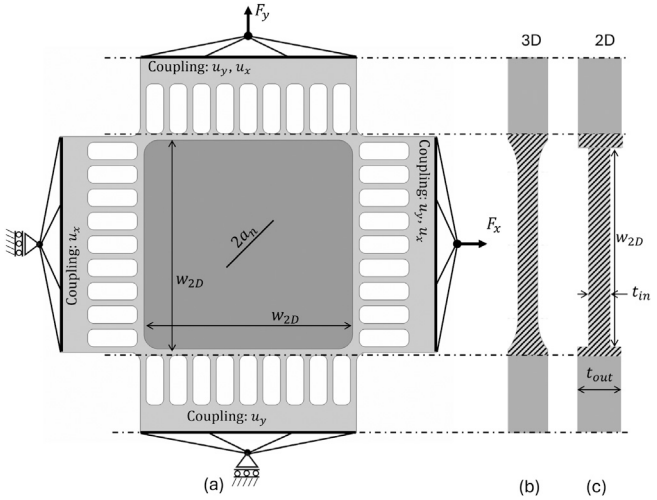

Fig. 4. Cruciform specimen [15,49]: (a) Front view of geometry, dark area indicating the measurement area with thickness t_{in} and width W_{2D} (b) Cross-section of 3D geometry (c) Cross-section of 2D geometry, approximation of 3D geometry with equal dashed area.

schematization of the used geometry. The slots are included to facilitate the decoupling of the two loading directions. The specimen is connected to the testing machine through a bolted connection, which is not shown in Fig. 4. Fig. 4(b) shows the cross-section of the specimen (Fig. 4(c) will be introduced later). A detailed technical drawing of this specimen is shown in [49]. A diagonal starter notch of length $2a_n$ is machined from a hole in the centre.

Wolf et al. [15] studied the effect of a phase shift in several experiments. In the current research, the focus is on two experiments, namely a biaxial load with a 22.5° phase shift, denoted with Experiment I, and a varying phase shift, denoted with Experiment II. These experiments are chosen because they resulted in non-straight crack paths without branching of the cracks. For Experiment I, the applied load consists of two stages, namely, an in-phase biaxial load stage resulting in a pure Mode-I load at the crack tip, followed by a load stage with a phase shift of $\phi_F = 22.5°$, corresponding to $t/16$, see Fig. 5(a). Fig. 5(b) shows the corresponding K_I and K_{II} directly before and after the change in load phase shift. The phase shift between K_I and K_{II}, ϕ_K, is a function of the phase shift of the applied load, ϕ_F, the crack length, and the FCGD. The phase shift and the biaxiality ratio at the change in load phase are $\phi_K = 90°$ degrees and $\Delta\lambda = 0.22$, respectively. Fig. 6(a) shows the experimental crack path [15], where subscript 0 indicates the end of the pre-crack and the subscript 1 indicates the change in load phase. The experiment is indicated by the superscript. The figure shows an abrupt and significant change in FCGD at a_1^I, even for the small biaxiality ratio. Thereafter, the FCGD gradually changes with increasing crack length. As both crack tips in the experiment show a similar FCGD as a function of crack size, the current study evaluates one crack tip.

Experiment II starts with an in-phase biaxial load resulting in a pure Mode-I load, similar as Experiment I. Subsequently, incremental phase shifts of $\phi_F = -15°$ degrees were applied until a final phase shift of $\phi_F = -90°$. Each load stage consists of a crack extension of approximately $\Delta a = 2\,\text{mm}$. Fig. 6(b) shows the experimental crack path [15] with the indicated stages where the occurrence of the change in load shift and its value are also indicated. The FCGD changes at each stage but remains approximately constant within a stage. The crack paths originating from each side of the machined notch show a similar trend.

2.1.2. Biaxial load with different load paths

Fremy et al. [42,43], Fremy [50] evaluated the effect of load paths on fatigue crack growth behaviour of stainless steel using cruciform specimens, see Fig. 7. Contrary to the experiments from [15], the specimens did not contain slots. In the experiments, the load was applied on all sides and controlled in such a way that the specimen remains centred throughout the load cycle. Therefore, no slots are needed. An initial notch of length $2a_n = 30\,\text{mm}$ was inserted in each specimen.

Fremy et al. [42] conducted mixed Mode-I and II experiments and mixed Mode-I and III experiments. The current study considers three of the mixed Mode-I and II experiments. All experiments have the same SIF ranges, but different load sequences, see Fig. 8. A positive Mode-I SIF is used to ensure crack opening at the start of the experiments, whereas the Mode-II SIF is fully reversed. Each specimen was pre-cracked to $2a_0 = 34\,\text{mm}$ before applying the mixed-mode load. The experiment results in different FCGR and different crack paths, visualized in [42]. Fig. 9 provides the FCGD obtained from a combination of photos and additional descriptions in [42]. Experiment A and B show co-planar crack growth for the first 1 mm crack extension. At a_1, after approximately 1 mm of crack extension, the crack in the Experiment A "in-phase" changes direction with $\theta_c \approx 40\,\text{deg}$. Experiment B "square" shows a smaller deviation angle, $\theta_c \approx 10\,\text{deg}$. A possible explanation provided by the authors from the current paper, for the sudden change in experimental FCGD is that the crack grows outside of the plastic zone of the pre-cracking procedure at crack size a_1. The plasticity influences crack closure and therefore the effective stress intensity factors are

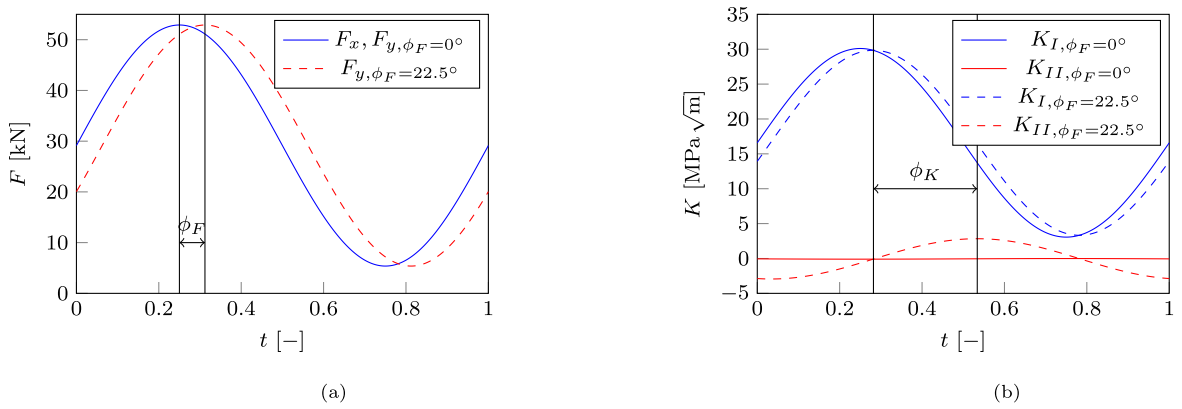

Fig. 5. Visualization of applied load in Experiment I [15]: (a) Load as function of time (b) SIF values directly before and after the change in load phase shift and the SIF phase shift, ϕ_K, for the cycle with $\phi_F = 22.5°$ as function of time.

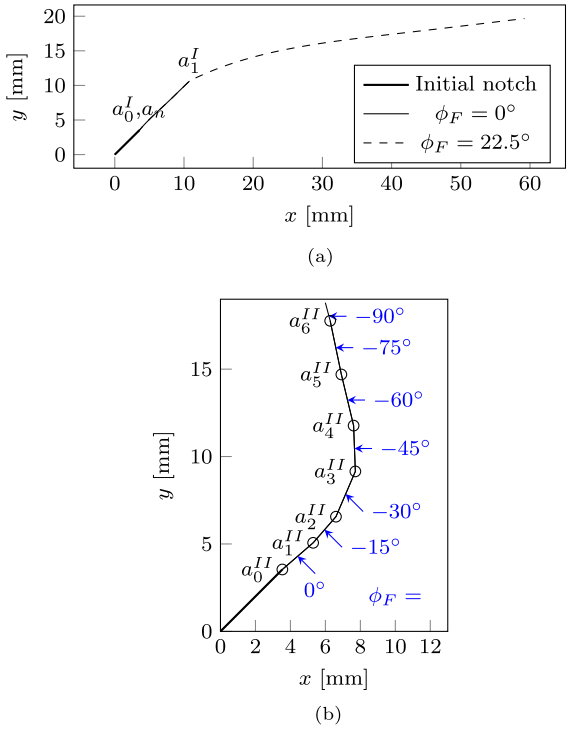

Fig. 6. Visualization of experimental crack paths [15]: (a) Experiment I, (b) Experiment II.

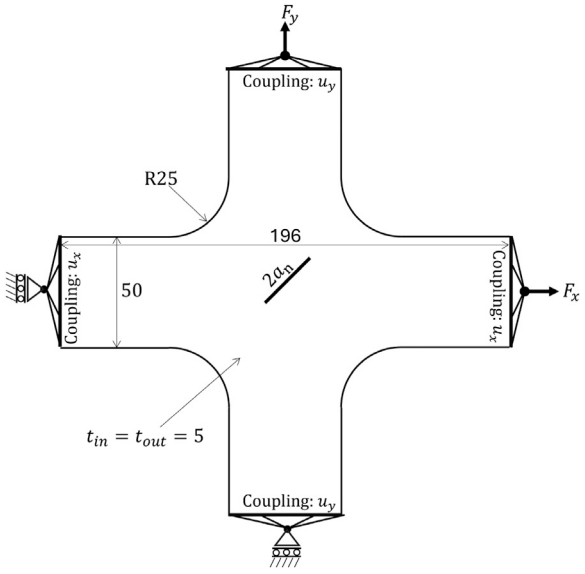

Fig. 7. Geometry used for Experiment A-C biaxial. Geometry based on [42]. All dimensions are in mm.

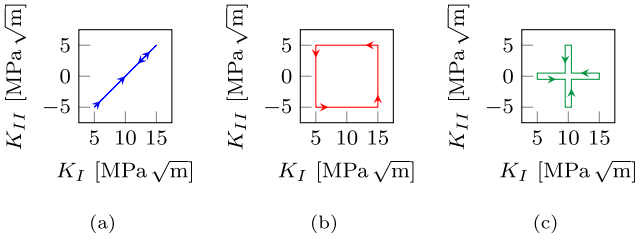

Fig. 8. Visualization of different loading paths in [42] all having the same K_I and K_{II} ranges: (a) Experiment A: "In-phase" (b) Experiment B: "Square" (c) Experiment C: "Cross".

different before and after the crack size a_1. However, further research is needed to substantiate this hypothesis. Experiment C "cross" shows co-planar crack growth throughout the entire crack path.

2.2. Fatigue crack growth direction criteria

This section describes the FCGD criteria defined in Table 1, which are used in this paper to model experiments described in Section 2.1.

2.2.1. Maximum tangential stress criterion

The MTS criterion is the most used criterion describing the FCGD in proportional load [26] and the direction in final fracture [51]. The MTS criterion states that the crack propagates in the direction perpendicular to the highest tangential stress σ_θ, assuming a polar coordinate system defined at the crack-tip, described mathematically by the angle that satisfies the following two conditions:

$$\frac{\partial \sigma_\theta}{\partial \theta_c} = 0, \quad \frac{\partial^2 \sigma_\theta}{\partial \theta_c^2} < 0 \tag{7}$$

In proportional load the angle of maximum tangential stress is equal to the angle in which the shear stress, $\tau_{r,\theta}$ is zero. Combining Eq. (1), Eq. (2), and Eq. (7), this results in a predicted crack growth angle for

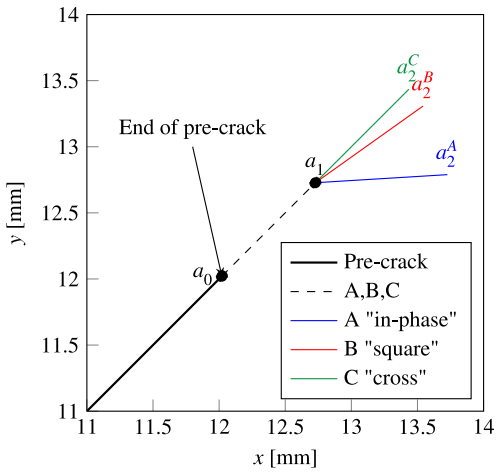

Fig. 9. Experimental crack paths of Experiments A-C [42].

proportional load:

$$\theta_c(t) = -\arccos\left(\frac{3\left[K_{II}(t)\right]^2 + \sqrt{\left[K_I(t)\right]^4 + 8\left[K_I(t)\right]^2\left[K_{II}(t)\right]^2}}{\left[K_I(t)\right]^2 + 9\left[K_{II}(t)\right]^2}\right) \tag{8}$$

for proportional load $\theta_c(t)$ is independent of time and evaluation of the direction is straightforward.

The MTS criterion is not uniquely defined in non-proportional load since it predicts a different angle for every time instance in the cycle. To account for the maximum SIF and the range of SIF, K_{max} and ΔK respectively, Highsmith [30] introduced a correction proposed by Walker for Mode-I fatigue crack growth. The predicted FCGD angle, θ_c, is the angle which maximizes the weighted product of the maximum SIF for an infinitely small increment, $K^r_{I,max}$ and the maximum corresponding SIF range, ΔK^r_I:

$$\begin{aligned}\theta_c &= \underset{\theta_c}{\operatorname{argmax}}\left[\Delta K_{I,w_c}(\theta_c)\right]\\ \Delta K_{I,w_c}(\theta_c) &= \left[K^r_{I,max}(\theta_c)\right]^{(1-w_c)}\cdot\left[\Delta K^r_I(\theta_c)\right]^{w_c}\end{aligned} \tag{9}$$

with

$$\begin{aligned}\Delta K^r_I(\theta_c) &= K^r_{I,max}(\theta_c) - K^r_{I,min}(\theta_c)\\ K^r_{I,max}(\theta_c) &= \max_t\left[\langle K^r_I(\theta_c,t)\rangle\right]\\ K^r_{I,min}(\theta_c) &= \min_t\left[\langle K^r_I(\theta_c,t)\rangle\right]\end{aligned} \tag{10}$$

In which $\langle\bullet\rangle = (\bullet + |\bullet|)/2$ are Macaulay brackets and w_c is a material constant [30], with value between zero and unity.

2.2.2. Maximum shear stress range

In some cases of RCF, Mode-II crack growth is observed without branching towards a Mode-I crack [20]. The plane of maximum shear stress corresponds to a co-planar direction in pure Mode-II, therefore Floros et al. [17] defined a criterion assuming that the FCGD aligns with the plane of maximum shear stress range, $\Delta\tau_{r\theta}$. Hence, the angle is defined as the angle that should satisfy the following conditions:

$$\frac{\partial\Delta\tau_{r\theta}}{\partial\theta_c} = 0, \quad \frac{\partial^2\Delta\tau_{r\theta}}{\partial\theta_c^2} < 0 \tag{11}$$

Contrary to Eq. (8), a simple closed form solution does not exist. Therefore, this criterion is numerically evaluated, and the predicted angle is based on the SIF solutions for an infinitely small crack increment using Eq. (1).

2.2.3. Vector crack tip displacement

The VCTD criterion predicts the direction of crack growth based on the displacement crack driving force. Li [52] developed this criterion for proportional load. The direction of crack growth for proportional load is given by:

$$\theta_c = \arcsin\left(\frac{\Delta\delta_{II}}{\Delta\delta}\right) \tag{12}$$

where $\Delta\delta_{II}$ and $\Delta\delta$ are the magnitude of the shear and total crack displacement ranges, respectively, see Fig. 10. A first order approximation of the displacement field around the crack tip is given by the Westergaard solutions [48,53]. Using this approximation, the following relation between SIF and crack tip displacement at a distance r from the crack tip is for Mode-I:

$$\begin{aligned}\delta_I(r) &= v^+(r) - v^-(r)\\ v^+(r) &= -v^-(r)\\ \delta_I(r) &= \frac{8K_I}{E'}\sqrt{\frac{r}{2\pi}}\end{aligned} \tag{13}$$

and similarly for Mode-II:

$$\begin{aligned}\delta_{II}(r) &= u^+(r) - u^-(r)\\ u^+(r) &= -u^-(r)\\ \delta_{II}(r) &= \frac{8K_{II}}{E'}\sqrt{\frac{r}{2\pi}}\end{aligned} \tag{14}$$

in which $u^{\pm}(r) = u\left(r,\theta_c = \pm\pi\right)$ and $v^{\pm}(r) = v\left(r,\theta_c = \pm\pi\right)$, see Fig. 10, and $E' = E$ for plane stress and $E' = E/(1-\nu^2)$ for plane strain.

Assuming that the direction of the Mode-I crack extension is co-planar with the original crack and that a Mode-II shear displacement leads to a Mode-II crack extension under 45 degrees, the total crack displacement, $\Delta\delta$ is given by:

$$\Delta\delta = \sqrt{\Delta\delta_I^2 + 2\Delta\delta_{II}^2 + 2\Delta\delta_I\Delta\delta_{II}} \tag{15}$$

Floros et al. [17,54] extended the VCTD to non-proportional load using an incremental evaluation of the VCTD. This led to the following expression of the resultant crack displacement:

$$\tilde{\delta}(t) = \sqrt{\left\langle\tilde{\delta}_I(t)\right\rangle^2 + 2\left\langle\tilde{\delta}_I(t)\right\rangle\left|\tilde{\delta}_{II}(t)\right| + 2\left[\tilde{\delta}_{II}(t)\right]^2} \tag{16}$$

the Macaulay brackets ensure contributions of only positive Mode-I displacements. The components $\tilde{\delta}_I(t)$ and $\tilde{\delta}_{II}(t)$ describe the fluctuation of the crack displacement. Following [17], this fluctuation is described by subtracting the mean displacements from the crack displacement components:

$$\begin{aligned}\tilde{\delta}_I(t) &= \delta_I(t) - 0.5\left[\max_t\left(\delta_I(t)\right) + \min_t\left(\delta_I(t)\right)\right]\\ \tilde{\delta}_{II}(t) &= \delta_{II}(t) - 0.5\left[\max_t\left(\delta_{II}(t)\right) + \min_t\left(\delta_{II}(t)\right)\right]\end{aligned} \tag{17}$$

By excluding the mean displacement, any permanent crack opening, for example resulting from plastic deformation, is disregarded in predicting the FCGD. The total vectorial crack increment, $\boldsymbol{\Delta a}$, for the evaluated load cycle is calculated as the maximum of the modulus of the two trial crack growth increments, $\boldsymbol{\Delta a}^+$ and $\boldsymbol{\Delta a}^-$:

$$\boldsymbol{\Delta a}^{\pm} = \int\left\langle\frac{\mathrm{d}\tilde{\delta}(t)}{\mathrm{d}t}\right\rangle f^{\pm}(t)\,\hat{\mathbf{e}}(t) \tag{18}$$

where $\hat{\mathbf{e}}(t)$ is the unit vector in the FCGD, $\theta_{VCTD}(t)$, at a specific instance of time, calculated with Eq. (19). This vectorial crack increment describes the crack extension in a local Cartesian coordinate system with an origin at the crack tip:

$$\hat{\mathbf{e}}(t) = \begin{bmatrix}\cos\left(\theta_{vctd}(t)\right)\\ \sin\left(\theta_{vctd}(t)\right)\end{bmatrix}, \text{ with } \theta_{vctd}(t) = \arcsin\left(\frac{\delta_{II}(t)}{\delta(t)}\right) \tag{19}$$

Essentially, this limits the crack growth to the increments in which the total crack displacement is increasing. The trial functions $f^+(t)$

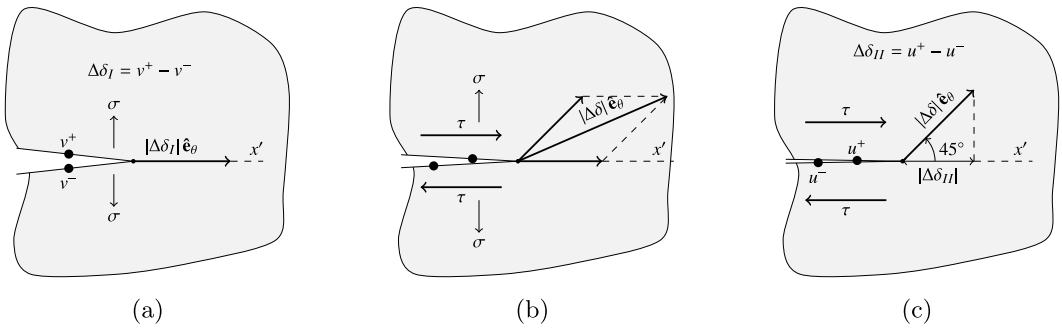

Fig. 10. Displacement definitions used in VCTD [52], $\hat{\mathbf{e}}_\theta$ is unit vector in the FCGD:(a) Pure mode-I load (b) Pure mode-II load (c) Mixed-mode load.

and $f^-(t)$ describe crack growth in respectively positive and negative direction with respect to the crack-tip:

$$f^+(t) = \begin{cases} 1, & \tilde{\delta}_{II}(t) \geq 0 \text{ or } \frac{\delta_I(t)}{|\tilde{\delta}_{II}(t)|} \geq \psi \\ 0, & \text{otherwise} \end{cases}$$
$$f^-(t) = \begin{cases} 1, & \tilde{\delta}_{II}(t) \leq 0 \text{ or } \frac{\delta_I(t)}{|\tilde{\delta}_{II}(t)|} \geq \psi \\ 0, & \text{otherwise} \end{cases} \tag{20}$$

in which $\psi \ll 1$ is a parameter describing locking in Mode-II crack growth, preventing crack growth in reversed shear load when the crack faces are in contact. Finally, the FCGD is determined by the direction of the total crack increment,

$$\theta_c = \arctan\left(\frac{\hat{e}_{\theta,y'}}{\hat{e}_{\theta,x'}}\right) \tag{21}$$

in which $\hat{\mathbf{e}}_\theta(t)$ is the unit vector in the predicted FCGD

$$\hat{\mathbf{e}}_\theta = \frac{\boldsymbol{\Delta a}}{\|\boldsymbol{\Delta a}\|}\ ,\ \hat{\mathbf{e}}_\theta = \begin{bmatrix} \hat{e}_{\theta,x'} \\ \hat{e}_{\theta,y'} \end{bmatrix} \tag{22}$$

The reader is referred to [17] for a comprehensive background of the methodology. Eq. (16) does not distinguish between crack opening due to plastic deformation and crack opening due to a positive static nominal Mode-I load. Therefore, deviating from the implementation in [17], an additional model variation is proposed here, referred to as VCTD*. Therefore Eq. (16) is replaced by:

$$\tilde{\delta}(t) = \sqrt{\overline{\langle\tilde{\delta}_I(t)\rangle}^2 + 2\overline{\langle\tilde{\delta}_I(t)\rangle}\,|\tilde{\delta}_{II}(t)| + 2\left[\tilde{\delta}_{II}(t)\right]^2} \tag{23}$$

in which $\overline{\langle\cdot\rangle}$ is a variation on the Macaulay bracket

$$\overline{\langle\tilde{\delta}_I(t)\rangle} = \begin{cases} \tilde{\delta}_I(t) & \text{if } \delta_I > 0 \\ 0 & \text{otherwise} \end{cases} \tag{24}$$

This implies that the Mode-I displacement fluctuation ($\tilde{\delta}_I$) contributes to the effectiveness of the cycle, if the total Mode-I displacement (δ_I) is positive, hence when the crack faces are open, by either plastic deformation or by a nominally applied Mode-I SIF. It is assumed that, if the VCTD method correctly describes the crack growth process in non-proportional load, reality is between the original VCTD and VCTD*.

2.2.4. Hourlier-Pineau criterion

Hourlier and Pineau [46] developed a criterion assuming that the FCGD is in the direction in which the SIFs of an infinitesimally small crack increment gives the highest FCGR. The highest FCGR corresponds to the highest equivalent SIF range. Following the methodology of [5], this is calculated with:

$$\Delta K^*_{eq}(\theta_c) = \left(\left[\Delta K^*_I(\theta_c)\right]^2 + \left(c_{II}\Delta K^*_{II}(\theta_c)\right)^2\right)^{0.5} \tag{25}$$

where c_{II} is a material constant, typically in the range 0.5–2 and should be tuned to experimental data. Subsequently the FCGD angle is predicted with:

$$\theta_c = \underset{\theta_c}{\text{argmax}}\left[\Delta K^*_{eq}(\theta_c)\right] \tag{26}$$

2.2.5. Minimum plastic zone radius

Golos and Wasiluk [47], Wasiluk and Golos [55] developed the minimum plastic zone radius (MPZR). This criterion assumes that the FCGD aligns with the minimum theoretical plastic zone radius around the crack tip. This is described by the angle that satisfies the following conditions:

$$\frac{\partial W}{\partial\theta_c} = 0, \quad \frac{\partial^2 W}{\partial\theta_c^2} > 0 \quad -\pi \leq \theta_c \leq \pi \tag{27}$$

in which W is the plastic zone radius normalized to the crack length. Since the crack length is constant during evaluation, this is the same as

$$\frac{\partial r_p}{\partial\theta_c} = 0, \quad \frac{\partial^2 r_p}{\partial\theta_c^2} > 0 \quad -\pi \leq \theta_c \leq \pi \tag{28}$$

in which r_p is an estimate for the plastic zone radius. Applying a von Mises yield criterion allows for estimating the elastic–plastic boundary. The von Mises yield criterion in cylindrical coordinates for plane stress conditions is given by:

$$\sigma_{ys} = \sqrt{\sigma_{rr}^2 - \sigma_{\theta\theta}\sigma_{rr} + \sigma_{\theta\theta}^2 + 3\tau_{r\theta}^2} \tag{29}$$

Substituting Eq. (2) into Eq. (29) defines the elastic–plastic boundary based on the von Mises criterion for plane stress conditions [56]:

$$\begin{aligned} r_p(\theta_c, t) = A\Bigg[& \left[K_I(t)\right]^2 \cos^2\frac{\theta_c}{2}\left(1 + 3\sin^2\frac{\theta_c}{2}\right) \\ & + K_I(t)K_{II}(t)\sin\theta_c\left(3\cos\theta_c - 1\right) \\ & + \left[K_{II}(t)\right]^2\left(3 + \sin^2\frac{\theta_c}{2}\left(1 - 9\cos^2\frac{\theta_c}{2}\right)\right)\Bigg] \end{aligned} \tag{30}$$

in which $A = 1/(2\pi\sigma_{ys}^2)$ is constant and is therefore omitted in the minimization. The criterion as developed by Wasiluk and Golos [55] is applicable for proportional load. In the current study, a proposal for non-proportional load is made, in which the shape of the plastic zone remains constant and is determined solely by the biaxiality ratio, λ, in proportional load. The plastic zone radii scale with the magnitude of applied load, but the minimum radius remains at the same angle. In non-proportional load, the shape changes due to the changing biaxiality ratio. It is proposed to create an envelope of the plastic zone field during a load cycle. Assuming no interaction in plasticity between the different time steps, the plastic zone radii envelope r_p^{max} is described by:

$$r_p^{max}(\theta_c) = \max_t\left[r_p(\theta_c, t)\right] \tag{31}$$

Subsequently, by combining Eqs. (28) and (31) the FCGD angle is predicted with:

$$\theta_c = \underset{\theta_c}{\text{argmin}}\left[r_p^{max}(\theta_c)\right] \tag{32}$$

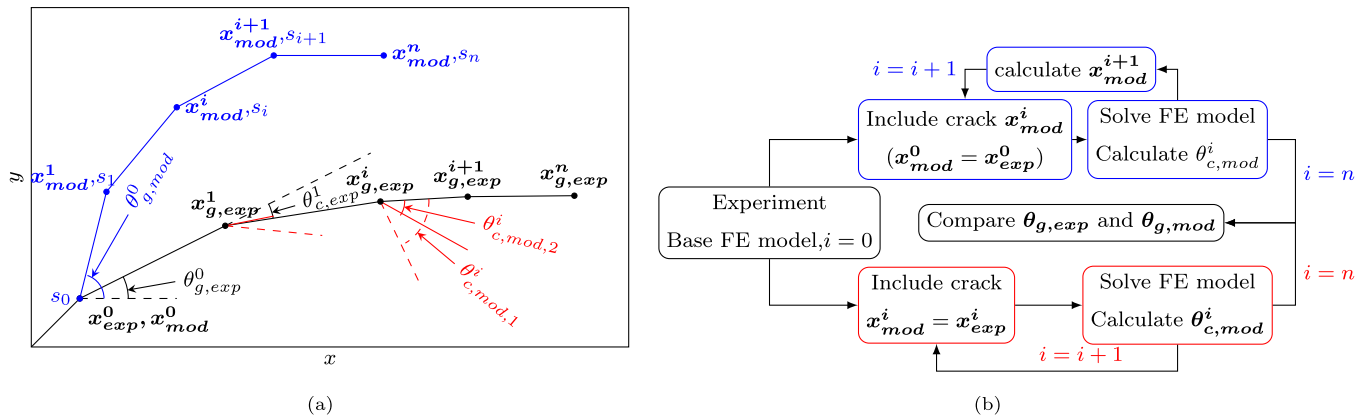

Fig. 11. Overview of the FCGD comparison scheme between experiment and prediction, blue: Comparison at specific experimental crack sizes; red: Incremental crack growth with predicted FCGD (a) Visualization (b) Flowchart.

3. Methodology

Fig. 11 shows the methodology used to evaluate the FCGD criteria. The crack driving forces are evaluated using the FE method. Two types of comparison with these criteria are carried out per experiment, namely, an incremental crack growth path in which the FCGD along the complete predicted crack path is compared to the experimental results (shown in blue in Fig. 11) and a comparison at specific crack sizes in the experiment (shown in red in Fig. 11). Vector $\boldsymbol{x}$ describes the crack path as a series of points $\boldsymbol{x}^i = [x_i, y_i]$ with x and y the cartesian coordinates according to Fig. 11(a). Based on these vectors, the angle in the global coordinate system is determined with:

$$\theta^i_g = \tan^{-1}\left(\frac{y^{i+1} - y^i}{x^{i+1} - x^i}\right) \tag{33}$$

The corresponding angle in the crack tip coordinate system is:

$$\theta^i_c = \theta^i_g - \theta^{i-1}_g \tag{34}$$

Similarly, the crack length, a, at a specific increment i is defined as the sum of the Euclidean distances between the different instances:

$$a^i = \sum_1^i \sqrt{\left(x^i - x^{i-1}\right)^2 + \left(y^i - y^{i-1}\right)^2} \tag{35}$$

3.1. Numerical model

Linear elastic FE models are used to derive SIFs given the geometry of the specimen and the load. The FE models are created in Abaqus [57]. All simulations files are added as supplementary material (https://zenodo.org/records/15807377). The cruciform specimens are idealized in 2-dimensional representations. To account for the non-uniform thickness in Experiment I and II, 2D elements with different thicknesses are assigned to different areas, similar as [15]. The measurement width, w_{2D}, is approximated assuming an equal area between the real, 3D, cross-section with the fillet and the 2D cross-section, indicated with the dashed area in Fig. 4(b) and Fig. 4(c). Comparison of the stress distribution and SIFs with a 3D FE model of the real geometry including the fillets shows that this 2D model gives a good approximation of the SIF values. The specimens in Experiment A, B and C have a uniform thickness and therefore all elements have the same (unit) thickness. The sides of the specimens are connected to the machine using a combination of bolts and clamps in all experiments. This is modelled by coupling the displacement of the edges of the specimen to reference points. On the left edge, only the translational degree of freedom (DOF) u_x is coupled to the corresponding DOF of the reference point u_{px}. Similarly, u_y is coupled to U_{px} on the bottom edge. The loads F_x and F_y are applied to the top and right edge, respectively. The displacements of these reference points are coupled to the displacements components of the nodes of that specific edge and these edges are prevented to rotate. Due to these coupling constraints, the right edge and top edge are prevented from contracting in respectively the vertical and horizontal direction, whereas the left and bottom edges are free to contract. Because of the slots, this asymmetric boundary condition has negligible influence on the calculated SIFs. For Experiment A, B and C the boundary conditions are symmetric, see Fig. 7. An initial crack with size $2a$ is inserted by duplicating the nodes and removing the connectivity between them. Quadratic quadrilateral plane stress elements are used with a full integration scheme. The mesh is refined to a mesh size of 0.1 mm in the vicinity of the crack tip and along the crack front. The mesh size is gradually increased to 2 mm outside this region to reduce the computational effort. A mesh sensitivity study on the calculated SIFs has been performed to establish these values. Fig. 12 shows an example of the mesh. A linear elastic isotropic material model is used, and the simulations are geometrically linear, assuming small deformations and rotations. For a sharp crack, the theoretical strain field at the crack tip in a FE model becomes singular. Using quadratic elements, this singularity is approximated by translating the mid side nodes to quarter point position close to the crack tip [58,59]. For every crack instance two unit load cases, F_x and F_y are simulated. Subsequently, superposition is used to calculate the SIF values at different time instances, to reduce the numerical complexity,

$$\begin{aligned} K_I(t) &= k_{I,x}F_x(t) + = k_{I,y}F_y(t) \\ K_{II}(t) &= k_{II,x}F_x(t) + = k_{II,y}F_y(t) \end{aligned} \tag{36}$$

in which k_{I,F_x}, k_{I,F_y}, k_{II,F_x} and k_{II,F_y} represent the Mode I and Mode II stress intensity factor components for unit load cases applied in the x- and y directions, respectively. In this study the SIF, is computed using the VCCT. In VCCT the SIFs are calculated by assuming that the energy required to advance the crack with a small increment is the same as the energy required to close the crack for the same increment, see [60–62]. The current implementation of the VCCT method has been validated in previous work [63].

3.2. Comparison fatigue crack growth direction

For the evaluation of the FCGD at individual instances in time, separate FE models are created with the crack path at the time instance following from the experiment $\boldsymbol{x}^i_{exp}$. The crack growth extension direction θ_c can be predicted in a post processing step.

A numerical procedure is used to calculate the FCGD angle. Depending on the criteria a quantity is maximized, (e.g. $\Delta K_{I,wc}$ in the MTS criterion, see Eq. (9)) or minimized (e.g. R_p^{max} in the MPZR criterion, see Eq. (32)). For some combinations of criterion, geometry and load, two

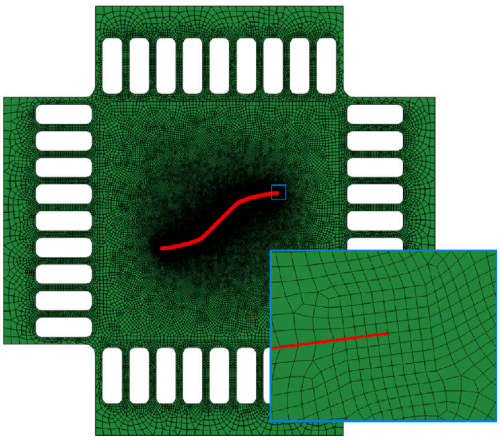

Fig. 12. Visualization of mesh in FE model used in Experiment I, red line indicates crack front. Inlet shows structured mesh used for VCCT method.

minima or maxima with approximately the same value are obtained for this quantity. Therefore, a threshold is set to avoid instability between the two approximately equal maxima or minima, as follows. If the difference between two local extremes is smaller than 1 %, they are both considered as potential FCGDs. It is assumed that non-homogeneous material behaviour results in a larger deviation than this threshold of 1 %.

3.3. Comparison of the crack path

An initial crack is inserted in the FE model for the comparison of the complete crack path, $\boldsymbol{x}^{\boldsymbol{0}}_{\boldsymbol{mod}}$, where superscript ^{0} indicates the starting crack in the experiment $\boldsymbol{x}^{\boldsymbol{0}}_{\boldsymbol{exp}}$, which is the crack dimension at the start of the evaluation, in this example at a_0. A crack extension angle $\theta_{c,mod}$ for the current increment is predicted using the considered criteria. Subsequently, the crack path is updated using this predicted angle and a fixed crack increment Δa. The sensitivity of the FCGD to Δa will be demonstrated later in this paper. The updated crack is inserted in the FE model and the procedure is repeated. The crack path prediction is stopped after a predefined number of steps. The predicted crack path is compared to the experimental crack path in terms of FCGD as a function of crack extension steps, s_i. A new set of FE models is used for every FCGD criterion.

3.4. Validation

In order to validate the FE model and the FCGD prediction algorithm, the results of the incremental crack growth procedure are compared to those of an experiment with proportional load from Miranda et al. [64]. This experiment is a crack growth test using a SEN(B) with a hole, see Fig. 13(a). Because of the hole, there is a proportional mixed-mode load at the crack-tip, in which the biaxiality changes continuously with crack length. A 2D plane stress FE model of the SEN(B) specimen is created. The load and boundary conditions are applied at single nodes. A linear elastic material model is used with $E = 205\,000$ MPa and $\nu = 0.3$. The FCGD is predicted using the MTS criterion, see Eq. (10), with $w_c = 1$ which corresponds to Eq. (8). Two different crack increments Δa are used. Fig. 13(b) shows the experimental crack path together with the predicted crack paths using the methodology described in Section 3.3. The figure shows that the predicted crack path is in good agreement with the experimental data and is independent of the crack increment. Because each experiment is unique, the presentation of the prediction differs per experiment.

4. Results

The predicted FCGD of the experiments outlined in Section 2.1 is presented in this section. The FCGD criteria introduced in Section 2.2 are assessed using the methodology from Section 3. Contrary to the validation case described in Section 3.4, in which the stress field changes spatially, the cruciform specimen used in the experiments in Section 2.1 are designed such that the stress field in the measurement area is approximately constant. Therefore, the crack path prediction results are presented in terms of FCGD angle as function of crack extensions steps.

4.1. Biaxial load with phase shifts

This section compares the crack path predicted with the considered criteria with the results of the experiments of [14,15] reported in Section 2.1.1. The FE model introduced in Section 3.1 has a measurement area with a width of $w_{2D} = 143$ mm and a nominal thickness, $t_{in} = 2$ mm, see Fig. 4. The outside area including the slots has a thickness, $t_{out} = 12$ mm. The experimental crack path is smoothened by fitting two fourth-order polynomial functions through the crack path for each of the two load stages, before adding it to the FE models. A linear elastic material model is used with $E = 192\,000$ MPa and $\nu = 0.24$ [14].

4.1.1. Experiment I: Fatigue crack growth direction

Fig. 14(a) shows the SIF, normalized with the square root of the crack length, over one load cycle at different experimental crack lengths. This normalization excludes the increase in SIF due to the increase in crack length and allows to show the change in SIF caused by the change in FCGD. The Mode-I SIF, K_I, is almost independent of the crack size, despite of the change in FCGD and the accompanying shift in SIF phase. The range of K_{II} decreases with increasing crack length. Initially, the Mode-II is fully reversed ($K_{II,mean} = 0$) and a negative $K_{II,mean}$ develops as the crack advances. The maximum plastic zone size is estimated with Eq. (30), using $\theta_c = 0$ and $\sigma_{ys} = 252$ MPa [15]. The ratio between the crack length and the calculated maximum plastic zone size estimated using Eq. (30) is between 5.5 and 7.0, depending on the crack length. The authors consider this ratio to be just large enough for the small scale yielding conditions that are a prerequisite of LEFM. Fig. 14(b) shows the phase change in SIF, ϕ_K and the biaxiality range $\Delta\lambda$ as function of the crack length. The latter increases to approximately 0.25 in the first mm crack growth after the application of the load phase change. Subsequently, this ratio reduces significantly with increasing crack length due to the reduction in K_{II}. As a result, the crack is Mode-I dominated towards the end of the experiment. The phase shift ϕ_K increases from $\phi_K = 90°$ at a_1^I to approximately $\phi_K = 120°$ at a_2^I and it remains almost constant thereafter.

Fig. 15 shows the predicted FCGD angle in the global coordinate system following the methodology of Section 3.2. As indicated in Section 2.1.1 the experiment results in an abrupt change in crack direction. The jump in θ_g at a_1^I is approximately $-18°$ to $\theta_g = 27°$ at the change in load phase, indicated with a_1^I. Subsequently, the angle decreases and stabilizes at approximately $\theta_g = 7°$.

For the MTS criterion, three values for w_c are used, namely, 0.1, 0.5 and 0.9 mm, to show the sensitivity of the FCGD to this parameter. Similarly, two parameters are used for the HP criterion, namely, one favouring Mode-I crack growth ($C_{II} = 0.9$) and one favouring Mode-II crack growth ($C_{II} = 1.2$). The MSSR criterion results in two angles with approximately the same maximum shear stress range, shown by the dashed curves. The FCGD prediction just after the load change at a_1^I is strongly influenced by the K_I component as the K_{II} is zero at the peak and trough of K_I. The MTS, HP and MPZR criteria predict co-planar crack growth at a_1. This is due to the resulting SIF phase shift, $\phi_K = 90°$, in combination with the low ΔK_{II} range. However, non-zero FCGD angles are predicted at larger crack lengths. Fig. 16 elaborates this difference between zero and non-zero crack tip angles,

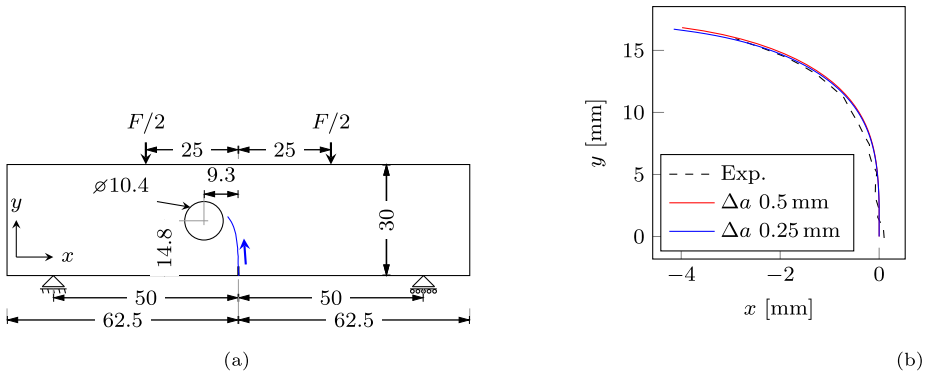

Fig. 13. Experimental crack path [64]: (a) SEN(B) Specimen, load configuration, experimental crack path and FE boundary conditions, all dimensions in mm (b) Predicted crack path using MTS criterion for two crack size increments, for clarity x and y-axis are not scaled equally.

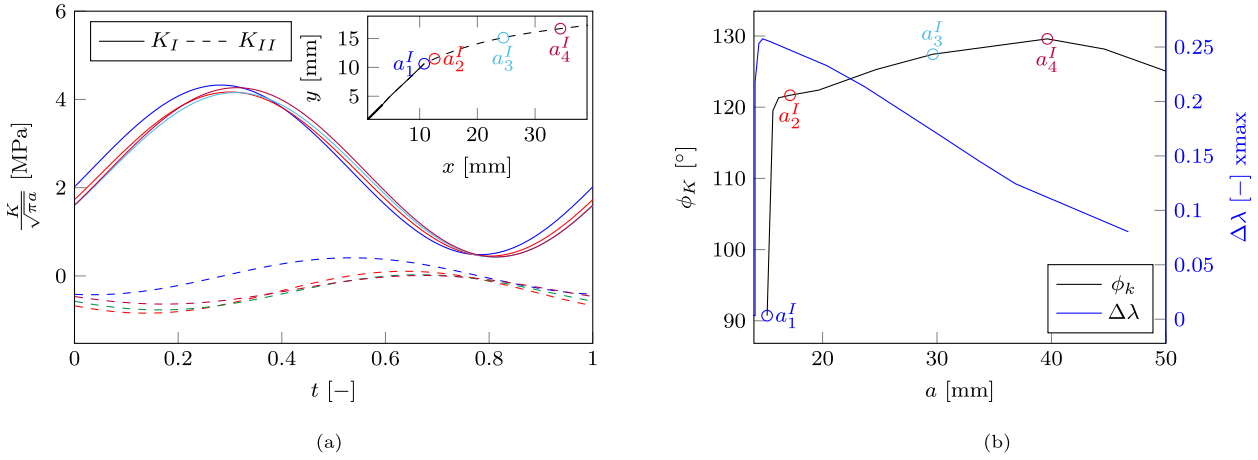

Fig. 14. SIFs for several instances for Experiment I: (a) K_I and K_{II} as function of time for different crack lengths (in mm) (b) Phase difference and biaxiality range as function of crack length.

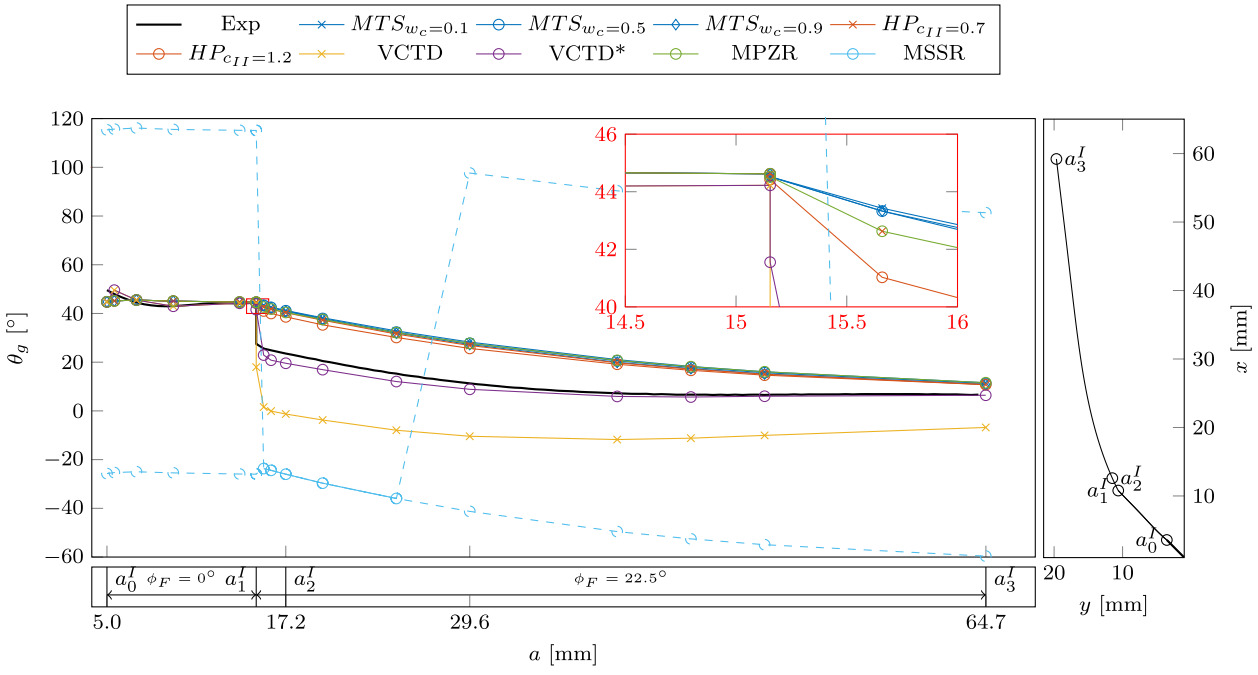

Fig. 15. Predicted crack extension angles for different crack growth criteria for Experiment I as function of the crack length.

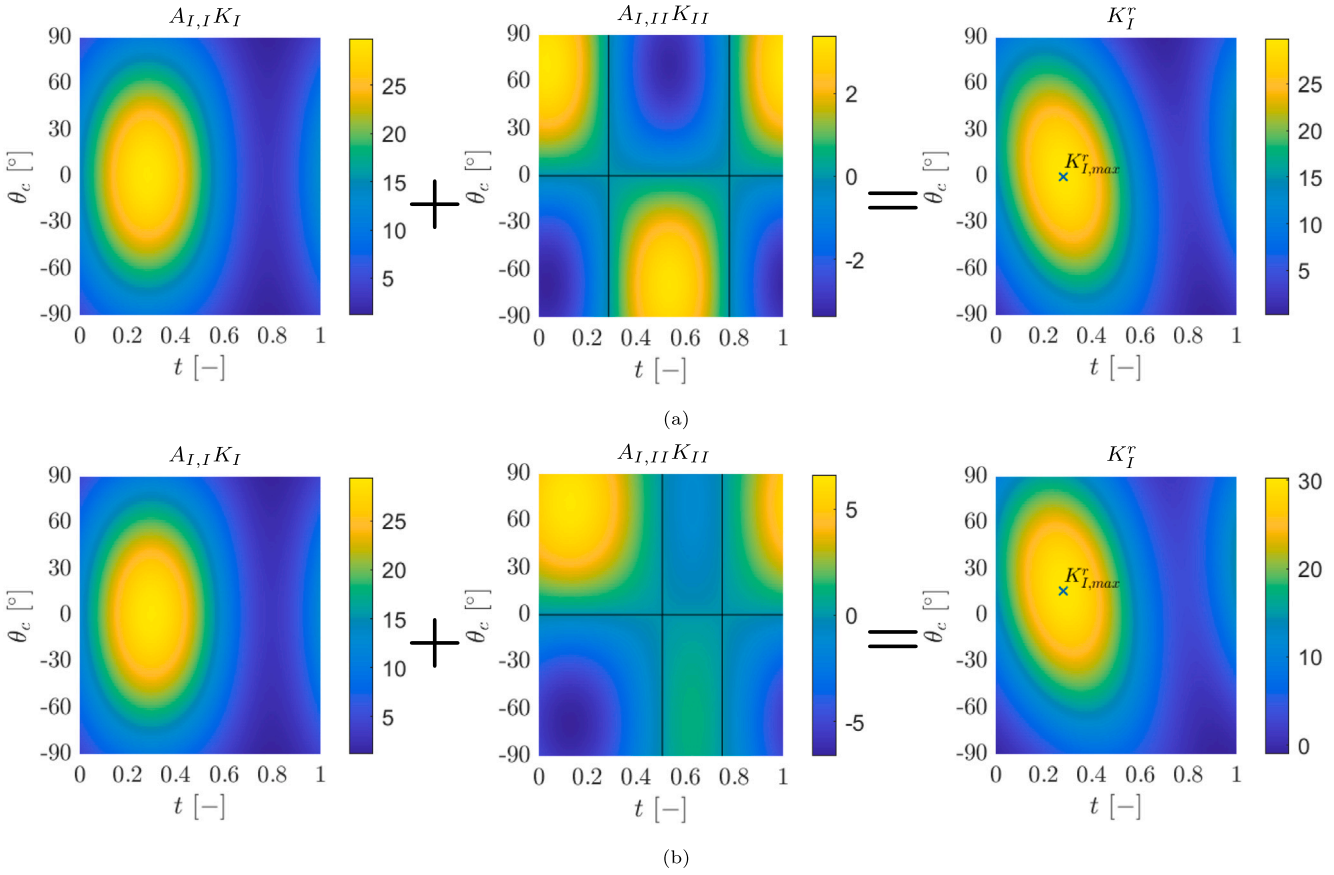

Fig. 16. Contribution of K_I and K_{II} on K^r for infinitely small crack extension around crack-tip, left: Mode-I contribution to K_I^r middle: Mode-II contribution to K_I^r, black lines denote zero contour, right: Total K_I^r, see Eq. (3). (a) Results corresponding to a crack length a_1^I. (b) Results corresponding to a crack length a_2^I.

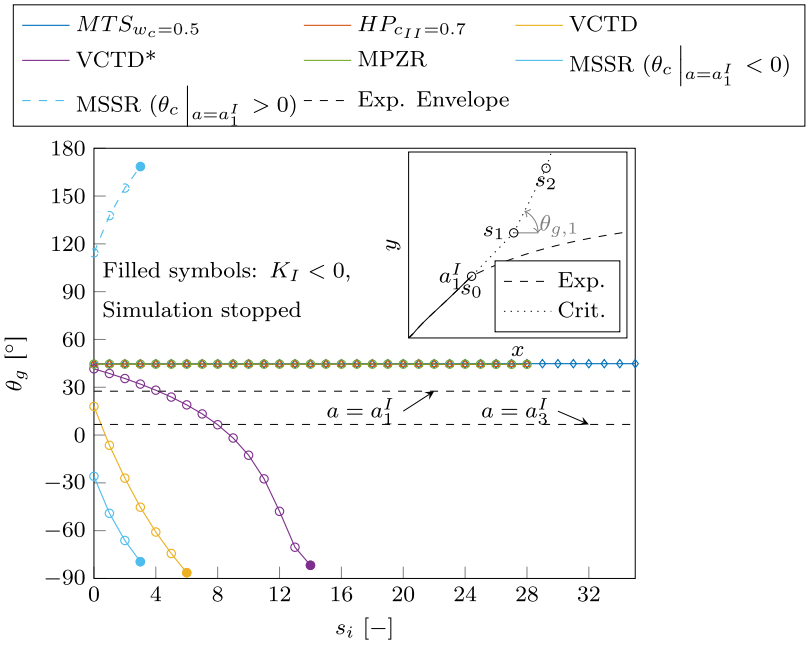

Fig. 17. Predicted FCGD angle for different crack growth criteria for Experiment I as function of crack extension steps. For definition a_3^I see Fig. 15.

θ_c. The figure shows the components of $K_{I,r}$ (see Eqs. (3) and (4)) as a function of θ_c during a cycle. The SIF for an infinitely small increment around the crack-tip $K_{I,r}$ (right figures) consists of a contribution of K_I (left figures) and a contribution of K_{II} (middle figures). Fig. 16(a) and (b) corresponds to crack length a_1^I and a_2^I respectively. For a_1^I, due to the phase shift $\phi_K = 90°$, the region of maximum $A_{I,I}K_I$ corresponds to a region where $A_{I,II}K_{II}$ is approximately zero. Therefore, the Mode-I component dominates the maximum K_I^r. Simulations with the MTS

criterion show that a Mode-II range of approximately 80 % of the Mode-I range would be needed to change the angle predicted for this phase shift $\phi_K = 90°$. Contrary, for a_2^I, the middle figure in Fig. 16(b) shows that the region of maximum $A_{I,II}K_{II}$ shifts in time. Consequently, at a_2^I, the maximum of K_I^r occurs at non-zero θ_c even for the relatively small value of $\Delta\lambda$. Note that the ratio between K_{II}^{min} and K_{II}^{max} influences the predicted FCGD in addition to the change in phase shift. This ratio is not displayed in the figure. The above derivation is conducted for the MTS criterion with a Walker coefficient of 0.0. Similar results follow for other Walker coefficients and for the HP and MPZR criterion. In the second load stage, $a > a_1^I$, the MTS criteria predict larger angles than the experiment with a marginal influence of the Walker coefficient w_c. Similarly, the HP criteria predict larger angles than the experiment. This implies that the MTS and HP criteria underestimate the effect of the Mode-II component. The MPZR predicts similar angles as the MTS criterion for this experiment.

The VCTD and VCTD* criteria predict a change in direction at the change in load phase. The FCGD angle of the VCTD* criterion agrees better with the experiment than the VCTD criterion. The difference in FCGD between these two criteria stems from a contribution of the Mode-I displacement during the whole cycle in the VCTD* criterion, thereby giving a larger contribution of Mode-I crack growth.

4.1.2. Experiment I: Crack path

Fig. 17 shows the FCGD angle as a function of the crack extension steps s_i starting at the crack length at the onset of the phase change, a_1^I. An increment size $\Delta a = 0.5\,\text{mm}$ is used in these simulations. The FCGD angle of the experiment gradually changes between $\theta_g = 7°$ and $\theta_g = 28°$ in the interval $a_1^I \leq a \leq a_3^I$, indicated with the dashed lines. Note that the crack driving forces, ΔK_I, ΔK_{II} and ϕ_k hardly change in this interval. Because Fig. 15 shows that the influence of w_c is limited, here only $w_c = 0.5$ is adopted for the MTS criterion. Similarly, $c_{II} = 0.7$ is used for the HP criterion. The HP, MPZR and MTS criteria predict an approximately equal and constant FCGD, independent of number of steps. In the first increment, the crack deflects towards the direction corresponding to the angle that maximizes the corresponding quantity (See Eq. (9), Eq. (25) and (31)). After this first increment, there is little influence of the geometry and the FCGD angle remains approximately constant. However, the predicted FCGD angle by these three criteria, $\theta_g = 45°$, corresponding to the orientation of the initial notch, is significantly larger than experimental value. Fig. 15 shows that the MSSR criterion predicts two equally likely angles for the first step, indicated in Fig. 17 by two curves. After the first increment, only a single FCGD angle is predicted in every step.

The VCTD, VCTD*, and MSSR criteria predict a FCGD which reduces with increasing number of crack extension steps, s_i. These criteria predict a FCGD that results in contact between the crack faces at the crack tip after a certain number of steps at certain part of the cycle. This is indicated with the filled symbols. Since contact between the crack faces is not included in the current modelling framework, the simulations are stopped after the corresponding increment. The resulting FCGD according to the VCTD, VCTD* and MSSR criteria depends on the number of simulated increments. Therefore, evaluation of the FCGD at a specific instance of time, as shown in Fig. 15, does not necessarily indicate the final predicted FCGD.

Fig. 18 shows the effect of the crack increment Δa on the FCGD. Three different increment sizes are used. Obviously, the HP criterion shows no influence of the crack increment as the predicted FCGD is straight and remains constant after the first step. Therefore, these simulations are stopped after respectively 12, 14 and 30 increments. The FCGD calculated with the VCTD* criterion is independent on the increment size for the first nine steps, but it differs for $s_i > 9$. The difference arises because the total crack extension becomes large with respect to the initial crack and the crack driving forces change. The simulations with $\Delta a = 0.1\,\text{mm}$ and $\Delta a = 0.2\,\text{mm}$ predict crack face contact at respectively 12 and 14 steps. However, the VCTD* criterion

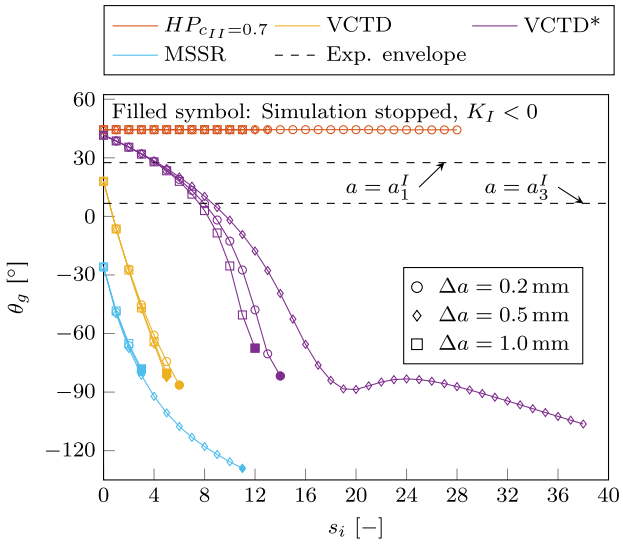

Fig. 18. Influence crack extension increment Δa on crack angle as function of crack extension steps for Experiment I. For definition of a_1^I and a_3^I see Fig. 15.

with $\Delta a = 1.0\,\text{mm}$ shows a different trend, where, K_I remains positive until the end of the simulation. This becomes evident from Fig. 19(a) which shows K_I as function of s_i. Fig. 19(b) shows the corresponding predicted crack paths. This clearly shows that if the predicted crack is large compared to the initial crack, it passes into the fourth quadrant (x^+, y^-) causing the different trend. The VCTD and MSSR criteria shows a similar trend, in which the predicted FCGD does not depend on the increment size but is does depend on the number of crack extension steps, s_i. This is in agreement with [65] where, they modelled an example of RCF using two increment sizes.

4.1.3. Experiment II: Fatigue crack growth direction

Fig. 20(a) shows the evolution of SIF during a single cycle for several crack lengths for Experiment II. These crack lengths correspond to the load phase changes shown in Fig. 20(b). The applied load phase shift, ϕ_F, decreases with increasing crack length. The biaxiality range first increases to approximately 0.4 at $\phi_F = -45°$, and thereafter, the further decrease of ϕ_F results in a decrease of $\Delta\lambda$. The graphs show that the applied load phase changes between $\phi_F = 0°$ and $\phi_F = -90°$ and that the phase shift in SIF changes between approximately $\phi_K = -50°$ and $\phi_K = -90°$. The ratio between crack length and the plastic zone is estimated between 6.5 and 7.5 for Experiment II. The authors hence assume the prerequisite of LEFM to be met.

Fig. 21 shows the FCGD in Experiment II. The crack path in this study is linearized within each stage. The experiment has an angle of $\theta_g \approx 41°$ at the start of the first stage. Therefore, despite of the zero phase load shift, a small Mode-II component arises in this stage. The MTS, MPZR and the HP criteria predict a FCGD angle close to $\theta_g = 45°$, because of this small Mode-II component. The predicted angles using these criteria are smaller than the experimental angles in the other load stages. Hence, these criteria underestimate the influence of Mode-II on the FCGD for this experiment.

The VCTD* criterion is closest to the experimental result. However, the abrupt changes in direction between the load stages are not captured. Similar to Experiment I, the MSSR criterion predicts two angles, this is due to the relatively small Mode-II component. Both angles disagree with the experimental angles. The MPZR criterion predicts angles similar to the MTS criterion, also in disagreement with the experiment.

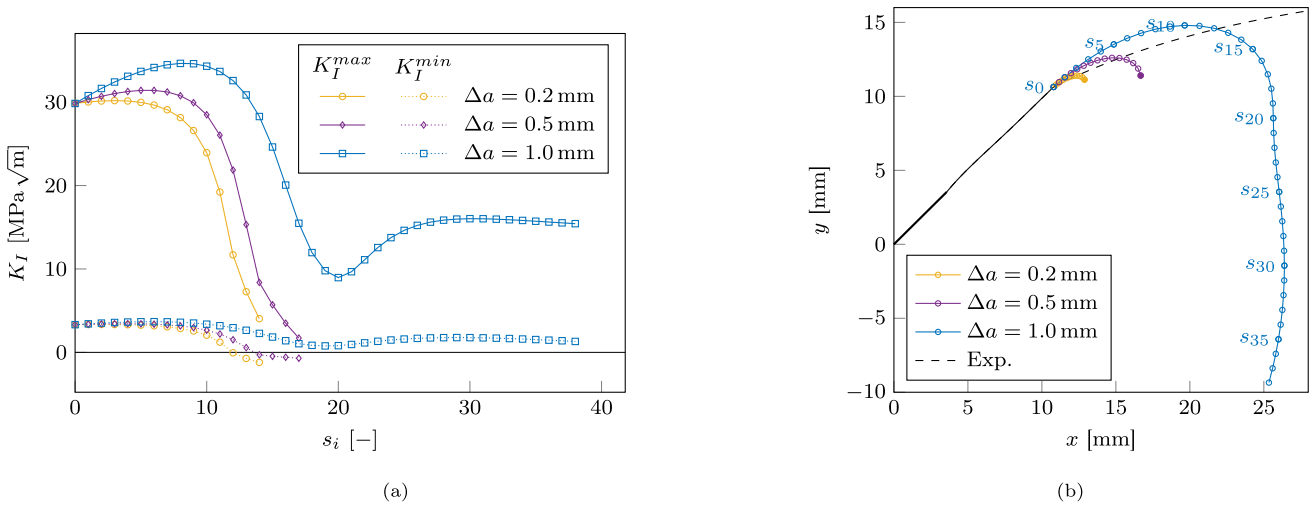

Fig. 19. Crack paths using the VCTD* criterion for Experiment I, for different crack extension increments Δa. (b) Maximum and minimum Mode-I SIF. (b) Crack path.

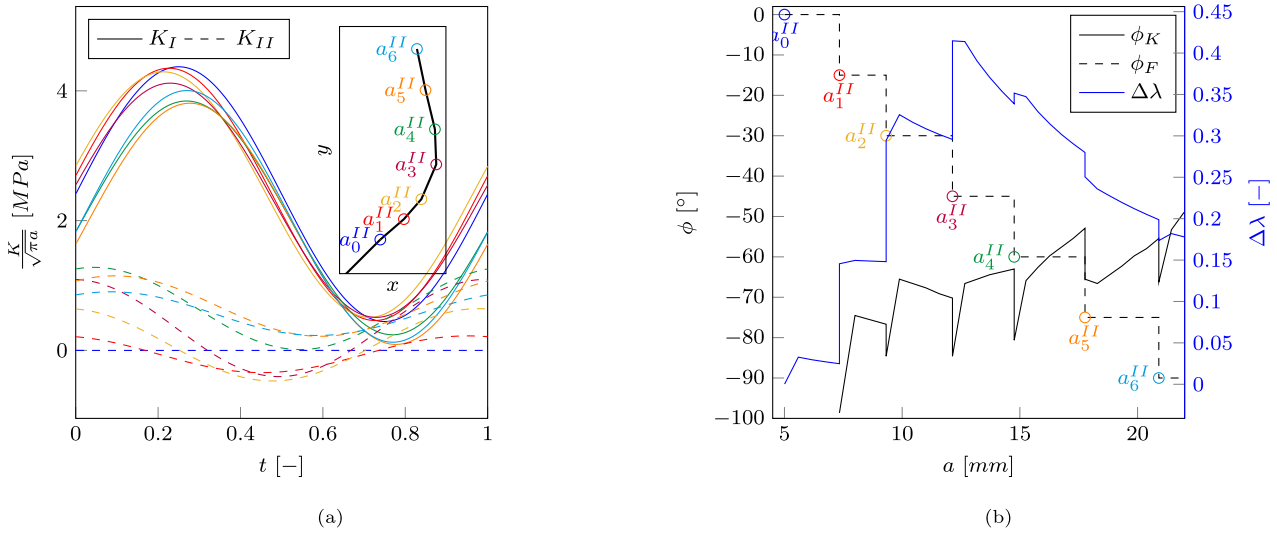

Fig. 20. SIFs for several instances for Experiment II: (a) K_I and K_{II} as function of time (b) Phase difference and biaxiality range as function of crack length.

4.1.4. Experiment II: Crack path

Fig. 22 shows the predicted FCGD for Experiment II. The crack growth simulations start at a_1^{II}, the first load stage with non-proportional load. A crack increment of $\Delta a = 0.5$ mm is used. Four simulation steps are made because this corresponds to 2 mm crack extension, which is approximately equal to the experimental crack extension between a_1^{II} and a_2^{II}. The experimental FCGD is constant between a_1^{II} and a_2^{II}.

The MTS, HP and MPZR criteria again predict an approximately equal and constant FCGD. The FCGD angle with respect to the global coordinate system, θ_g, predicted by the MTS and HP criteria is smaller than the experiment. The VCTD predicts an angle θ_g which increases with an increasing number of steps, diverging from the predicted experimental angle. The VCTD* criterion predicts an increasing angle with an increasing number of extension steps. The final crack length after four increments is relatively close to the experimental FCGD.

Fig. 23(a) shows the effect of crack increment size for the MTS, HP, VCTD* and MSSR criteria. The simulations are performed for the stage between a_3^{II} and a_4^{II}, as in this stage all criteria predict non-zero angles, see Fig. 21. The experimental FCGD is constant in this stage. Like Experiment I the MTS and the MPZR criteria predict an approximately constant FCGD independent of the crack increment size. However, the angle is significantly smaller than the experimental value. The HP criterion predicts an angle which is again relatively independent of the increment size. After 10 crack extension steps, the maximum difference in θ_g is 5°. The VCTD criterion predicts a similar FCGD for both increment sizes in the first two crack extension steps. However, the angle is significantly larger than in the experiment. The VCTD* criterion predicts a FCGD that is also approximately independent of crack increment size. As in Experiment I, the FCGD predicted by the VCTD*, is closer to the experimental value compared to the VCTD criterion. The MSSR criterion is closest to the experimental value for the first crack increment. However Fig. 21 shows that the VCTD* criterion is closer to the experimental values over the entire crack path.

Prediction of the crack path not only requires an estimate of the FCGD, but also the FCGR. Therefore, for the simulations shown in Fig. 23 the FCGR is estimated. Wolf et al. [14] measured the FCGR in the different stages of the experiment, showing that the data correspond to a Paris law [66] with a slope parameter $m = 2.40$:

$$\frac{\mathrm{d}a}{\mathrm{d}N} = C\left(\Delta K_{eq}\right)^m \tag{37}$$

The equivalent SIF, K_{eq}, is calculated according to Wolf et al. [14].

$$K_{eq}(t) = \frac{K_I(t)}{2} + \frac{1}{2}\sqrt{\left[K_I(t)\right]^2 + 4\left[C_{II}K_{II}(t)\right]^2} \tag{38}$$

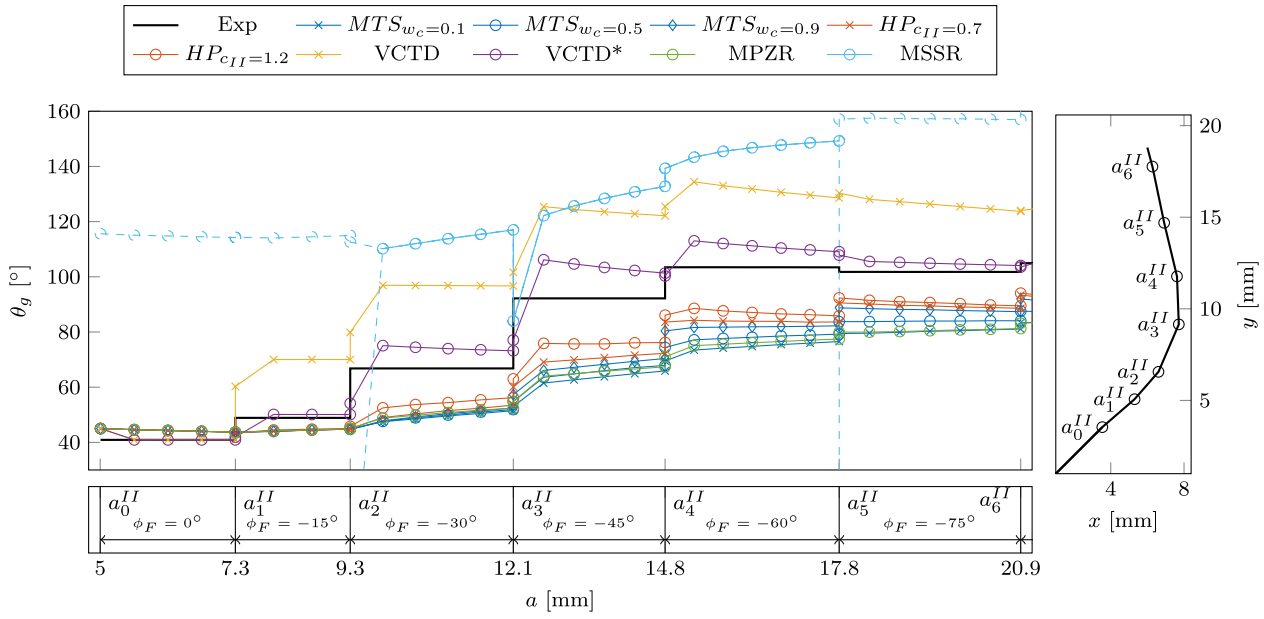

Fig. 21. Predicted crack extension angles for different crack growth criteria for Experiment II as function of the crack length.

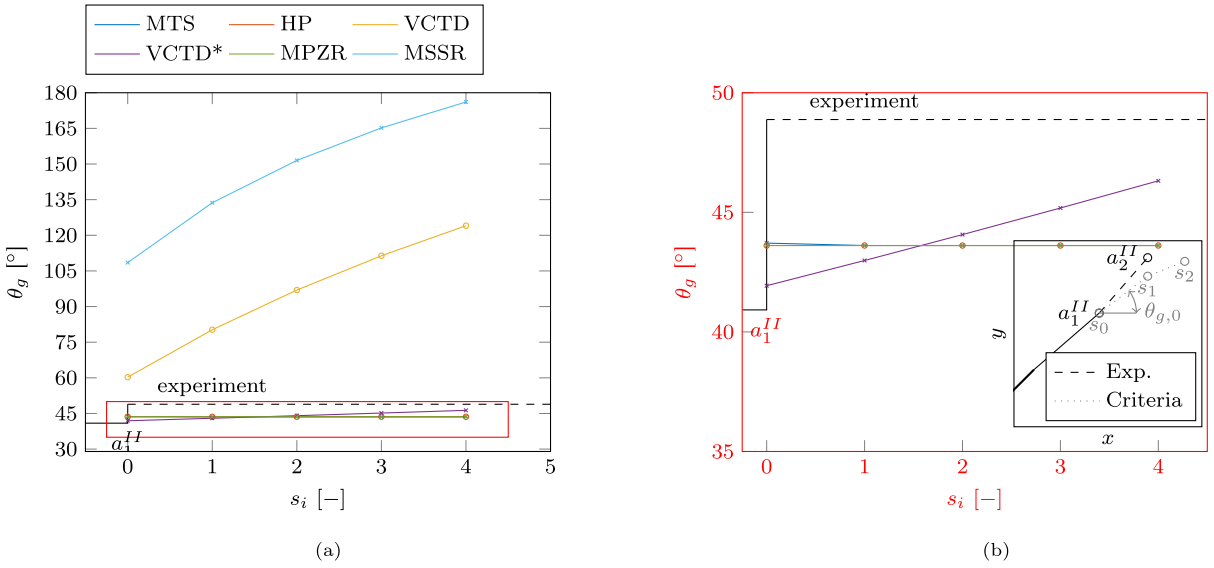

Fig. 22. Predicted FCGD angle for different crack growth criteria for Experiment II as function of crack extension. (a) Overview (b) Zoomed-in.

with $C_{II} = 1.155$, and:

$$\begin{aligned} K_{eq}^{max} &= \max_t \left[K^{eq}(t)\right] \\ K_{eq}^{min} &= \min_t \left[K^{eq}(t)\right] \\ \Delta K_{eq} &= K_{eq}^{max} - K_{eq}^{min} \end{aligned} \tag{39}$$

Fig. 23(b) shows the predicted FCGR using the Paris law fitted to the experimental data as a function of the crack extension between a_3^{II} and the current crack tip a_c^{II}. The FCGR is normalized with the FCGR at a_3^{II}. The experiment initially shows an approximately constant FCGR. This is a result of the change in FCGD angle from $\theta_g = 66°$ to $\theta_g = 91°$. As expected, the experiment shows an increasing FCGR with increasing crack length. The MTS, HP and MPZR criteria also predict an increase in FCGR. The VCTD and VCTD* criteria both predict a decrease in FCGR with increasing crack length. After two increments, the FCGR is reduced with approximately 30 %. If this reduction would continue, this would imply that the crack would arrest, which is not seen in the experiments.

4.2. Biaxial load with different load paths

This section compares the results of the crack path predicted with the different FCGD criteria with the results of the experiments of [42] reported in Section 2.1.2. Fig. 7 shows the geometry used in the analyses. A linear elastic material model is used with $E = 193\,000$ MPa and $\nu = 0.3$ [42]. Because of the limited information provided in the original source, the crack paths are described by linear segments between a_0, a_1 and a_2.

4.2.1. Experiments A-C: Fatigue crack growth direction

Fig. 24 shows the evolution of K_I versus K_{II} for three different crack lengths, namely, the length after pre-cracking, a_0, the length after 1 mm of mixed-mode crack growth, a_1, corresponding to the point of crack deflection in Experiment A and B, and the length after 2 mm of mixed-mode crack growth, a_2. The inserts show the corresponding

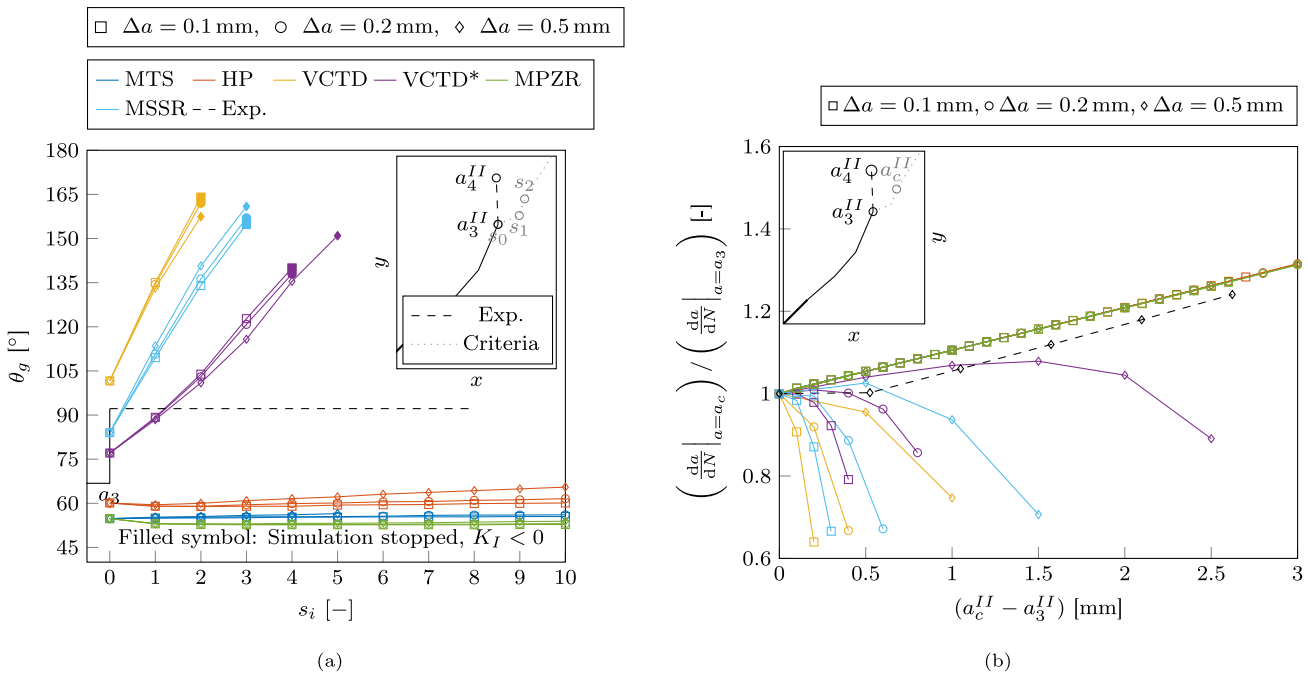

Fig. 23. Influence crack extension increment Δa in Experiment II: (a) Predicted crack path (b) Crack angle as a function of crack length.

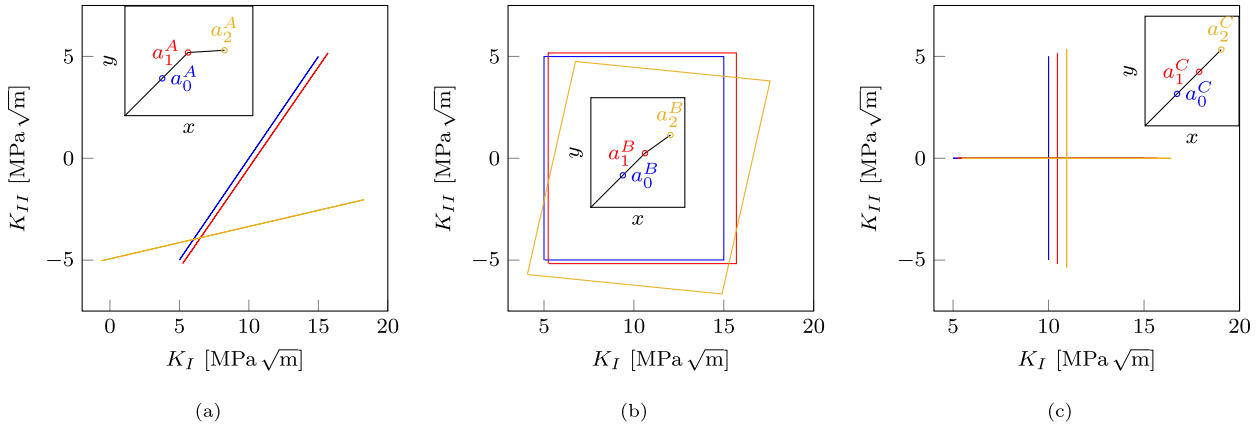

Fig. 24. K_I vs K_{II} for specific crack lengths of Experiments A-C, inset shows corresponding experimentally measured crack orientation: (a) Experiment A "in-phase" (b) Experiment B "square" (c) Experiment C "cross".

crack orientations. Conflicting information is given in [42,43] concerning the applied loads and the SIFs. The current FE simulations give relations between loads and SIFs that differ from the parametric relations given in [42,43], but which correspond with some graphs provided in [42]. Moreover, the relations of the current FE simulation agree reasonably with those in [67], in which similar specimens were analysed by the research group of [42,43]. The ratio between the provided SIFs in [67] and the calculated SIFs in this study are virtually independent of the crack length. Therefore, the current authors assume their modelling approach to be corrected and the SIFs in the current study are scaled to match the presented SIF history of $\Delta K = 10\,\text{MPa}\sqrt{\text{m}}$ [42] for an initial crack length a_0. The ratio between the crack length and the maximum plastic zone size, calculated with Eq. (30) and $\sigma_{ys} = 352\,\text{MPa}$ [68], is larger than 30 for Experiment A,B and C, conforming to small scale yielding condition so that LEFM can be used. The load is in phase for Experiment A "in-phase", hence explaining the straight lines in the plot. However, the ratio between K_I and K_{II} changes significantly after the change in FCGD. The Mode-I SIF range increases and the Mode-I mean SIF reduces, resulting in a negative Mode-I component during a part of the cycle. In the evaluation, it is assumed that there is full contact in compression hence K_I is taken equal to 0 in this region. The effect of this simplification is assumed negligible because it applies to a small fraction of the complete cycle only (< 4%). Both the Mode-II mean SIF and SIF range reduce significantly between the original orientation of the crack and the orientation after 1 mm of mixed-mode crack growth. The crack changes towards a Mode-I dominated crack. Experiment B "square" shows a slight increase in Mode-I and Mode-II SIF range after the first millimetre of mixed-mode crack growth. The cyclic Mode-I and Mode-II SIFs are initially decoupled, i.e. $\frac{\partial K_{II}}{\partial t} = 0$ if $\frac{\partial K_I}{\partial t} \neq 0$ and vice versa. However, a small interaction between the modes is observed after the directional change of the crack $a > a_1^B$. Experiment C "cross" shows a small increase in ΔK_I and ΔK_{II} with increasing crack size. The Mode-I mean SIF increases whereas the Mode-II mean SIF remain approximately constant. Similar to Experiment B the cyclic Mode-I and

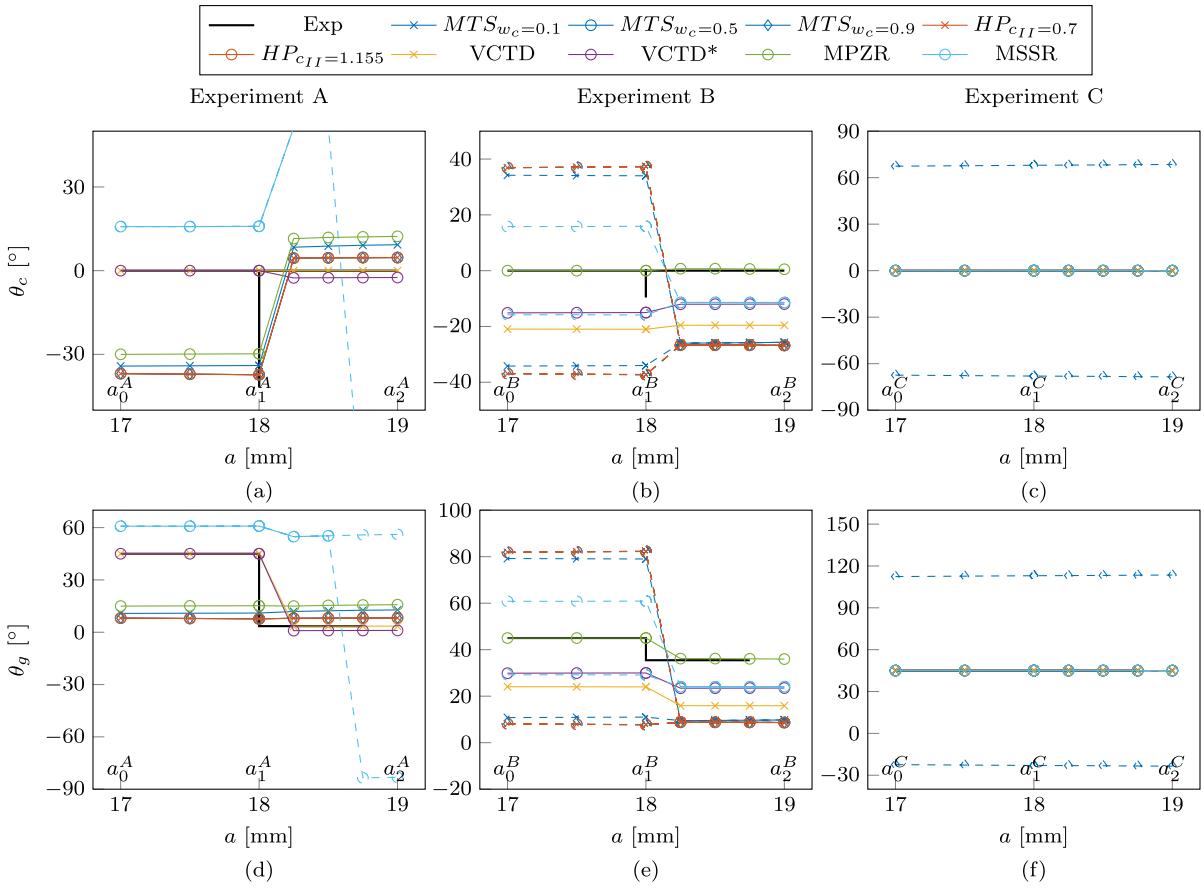

Fig. 25. Predicted crack extension angles for different crack growth criteria for Experiment A-C: (a) Experiment A "in-phase", crack tip coordinate system (b) Experiment B "square", crack tip coordinate system (c) Experiment C "cross", crack tip coordinate system (d) Experiment A "in-phase", global coordinate system (e) Experiment B "square", global coordinate system (f) Experiment C "cross" global coordinate system.

Mode-II SIFs are decoupled, but contrary to Experiment B "square", the range in one direction is applied at the mean SIF in the other direction.

Fig. 25 shows the predicted FCGD using different criteria as a function of the experimental crack length. Fig. 25(a–c) shows the FCGD angle in the crack-tip coordinate system and Fig. 25(d–f) shows the corresponding angle in the global coordinate system. As the crack paths are linearized, a single non-zero FCGD angle is displayed in this figure, indicating the change in the experimental crack path at a_1^A and a_1^B. The predicted FCGD between a_0 and a_1 remains constant for each of the criteria because the SIFs remain approximately constant. It is observed that the HP and MTS criteria predict a FCGD angle close to the experimental FCGD angle between a_1^A and a_2^A. On the contrary, the FCGD between a_0^A and a_1^A is not predicted well. Again, the MPZR criterion predicts similar angles as the MTS criterion. The VCTD criterion predicts a FCGD angle of zero degree for Experiment A "in-phase". This is a consequence of the subtraction of the mean displacement. The VCTD* predicts a small negative angle after a_2^A.

The MTS, HP, and the MSSR criteria do not predict a unique angle for the first three crack extensions in Experiment B "square", which is a result of the zero mean K_{II}. Consequently, two maxima of $K^r_{I,max}$ occur for two angles, corresponding to $K_I = 15\,\text{MPa}\sqrt{\text{m}}$ and $K_{II} = \pm 5\,\text{MPa}\sqrt{\text{m}}$, at times denoted as t^+ and t^-. These are the times of maximum $K_I^r(\theta_c, t)$, see Eq. (3).

Fig. 26(a) shows the individual components of K_I^r for the two time instances at a_1^B. Fig. 26(b) shows the same data for a crack length of $a = 18.25\,\text{mm}$, just after a_1^B. Two competing effects occur at this crack size, namely, $K_I(t^+) > K_I(t^-)$ which leads to a preference of t^+ and $A_{I,II}K_{II}(t^-) > A_{I,II}K_{II}(t^+)$ which leads to a preference of t^-. In this specific example, the first effect is stronger and the predicted angle is therefore uniquely defined corresponding to t^+. The above evaluation is done for $w_c = 0$, however, a similar evaluation can be made for non-zero w_c.

All criteria except MPZR predict non-straight crack growth for the initial phase of Experiment B. The straight crack predicted by the MPZR criterion is a consequence of the decoupling of Mode-I and Mode-II. Fig. 27(a) shows the theoretical plastic zone, calculated with Eq. (30), at the two previously defined time instances and a crack length a_1^B. The minimum of the envelope occurs at zero degrees, however, the local plastic zone size of both time steps is minimal at approximately ±30°. The MPZR criterion predicts a small positive θ_c after the change in experimental FCGD angle. This agrees reasonably with the experimental results. The HP criterion underestimates the FCGD angle significantly, see Fig. 25(b) and (e).

Most criteria predict straight crack growth for Experiment C "cross", which is in line with the experimental results. However, the MTS criterion with $w_c = 0.9$ predicts a non-zero angle of approximately 69° see Fig. 25c and f. To demonstrate the cause of this, Fig. 27(b) shows the Mode-I SIF range including Walker correction, $\Delta K_{I,wc}$, as a function of the crack extension angle. The MTS criterion is based on maximization of $\Delta K_{I,wc}$, see Section 2.2.1. The figure shows that there are three local maxima at $\theta_c = 0°$ and $\theta_c \approx \pm 69°$, for the three evaluated Walker constants. The largest of these three local maxima depends on the Walker constant.

In conclusion, none of the criteria is able to accurately predict the FCGD for all three experiments.

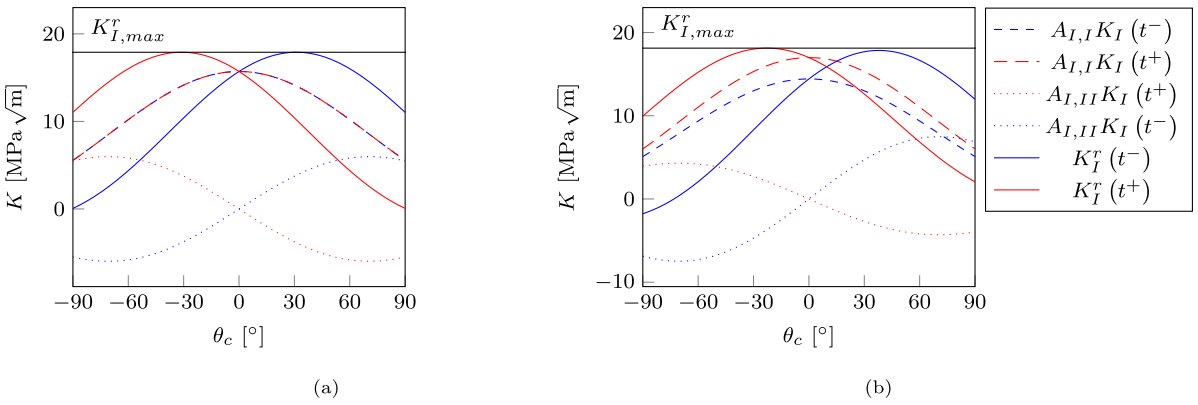

Fig. 26. Individual components of K^r_I for Experiment B "square". (a) At crack length $a^B_1 = 18\,\text{mm}$ (b) at crack length $a = 18.25\,\text{mm}$, just larger than a^B_1.

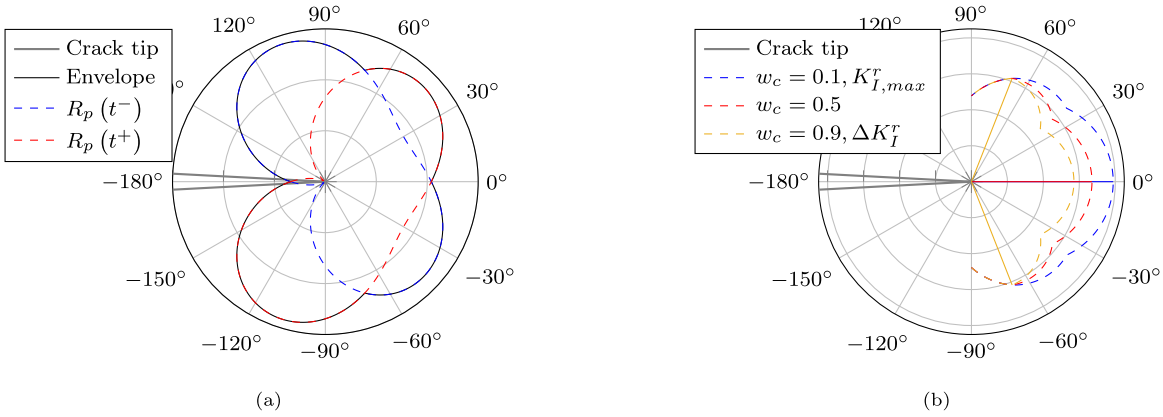

Fig. 27. Effects of crack tip plasticity in Experiments B "square" and C "cross" (a) Evaluation of plastic zone size at two time steps and a crack length $a = 18\,\text{mm}$ for Experiment B "square". (b) Influence of Walker constant w_c on predicted FCGD angle in the MTS criterion for Experiment C "cross".

5. Discussion

5.1. Fatigue crack growth direction

Different FCGD criteria result in a large envelope of predicted angles. The MTS, HP and MPZR criteria predict similar angles for most of the studied experiments. These predicted angles strongly depend on the SIF phase shift. It is shown that a SIF phase shift of approximately 90°, with a small to moderate Mode-II component ($\Delta\lambda < 0.8$), results in straight crack growth prediction (for example the FCGD angle at a^I_1 in Fig. 15 and the FCGD angle at a^{II}_1 in Fig. 21). However, they do not comply with the experimental results. On the other hand, FCGD predictions with larger ΔK_{II} components (for example, the start of Experiment B "square", Fig. 25b) showed the opposite behaviour. In these cases, the MTS and HP criteria predict non-zero FCGD angles whereas the experiment shows straight crack growth [42]. Since [42] applied discrete load changes instead of a continuous (e.g. sinusoidal) signal, the phase shift is undefined. However, one could consider Experiment B as subjected to $\phi_K = 90°$, see Fig. 28(a). Experiment B can then be compared to Experiment I, which for a just larger than a^I_1 is also subjected to $\phi_K = 90°$, see Fig. 14(b). The mean Mode-I SIF is equal to the Mode-I SIF range in Experiment B, whereas it is approximately equal to half the Mode-I SIF range in Experiment I. More importantly, the biaxiality range, $\Delta\lambda$ in Experiment B equals 1.0, whereas $\Delta\lambda \approx 0.2$ for Experiment I. Fig. 28(b) shows the effect of the biaxiality ratio on the FCGD using the MTS criterion for $\phi_K = 90°$ and different Walker coefficients. For Experiment B, it can be seen that for any non-zero Walker coefficient a non-zero FCGD angle is predicted. A zero Walker coefficient gives $\theta_c = 0$, in line with Experiment B at a^B_0. However, this does not explain the change in FCGD at a^B_1. For Experiment-I a zero FCGD angle is predicted if $\Delta\lambda < 0.8$, independent of the Walker coefficient. Hence, using the MTS criterion, there is no unique Walker coefficient able to correctly predict the FCGD of both experiments.

The MSSR criterion often predicts two angles with the same maximum shear stress (see Eq. (11)). Further research could be done to define an additional condition distinguishing between these angles. The VCTD criterion predicts a larger change in FCGD than most experiments. The VCTD* criterion predicts a smaller change in FCGD than the VCTD as the contribution of the Mode-I displacement is increased, which reduces the influence of the Mode-II displacements. Literature shows that the VCTD criterion can predict FCGD of some specific non-proportional experiments [54], showing its potential.

The current research is based on LEFM and linear elastic FE models. Therefore, the focus is on experiments with a positive K_I over the complete cycle, to minimize plasticity effects such as crack closure. However, crack closure is also found for low but positive K_I values in literature [69,70]. Therefore, it is possible that part of the discrepancy between experimental and predicted FCGD is attributed to the effect of crack closure. Both PICC and RICC have an effect on the effective SIFs. The effect on the effective Mode-II SIF is unknown. A consequence of the assumed linear elastic material behaviour is that the stress history does not influence the predicted FCGD, which simplified the evaluation of the chosen criterion significantly. Incorporating the effect of plasticity in a FCGD prediction is therefore crucial, but complex. The method developed by Pommier et al. [41–44] accounts for plasticity effects and aims to predict the FCGR. Through experiments, it is anticipated that the FCGD can be calibrated using their elastic–plastic crack driving force. However, dedicated experiments are required for

this purpose. It is suggested to first conduct proportional mixed-mode experiments at various biaxiality ratios. In the analysis, the plasticity developed due to pre-cracking needs to be considered to better understand the sudden change in FCGD in Experiments A-C. Subsequently, the non-proportional tests can be evaluated to provide more insight in the underlying mechanisms driving the crack under non proportional conditions.

The current evaluation is limited to constant amplitude load, already showing big challenges. In variable amplitude load, the effect of plasticity is more complex. In addition, evaluations of variable amplitude load require the value of the threshold of the SIF range. This value is not available for a given mode-mixity. Therefore, we expect that predicting the FCGD in variable amplitude load is even more difficult.

5.2. Crack path

Prediction of the crack path requires predictions of the FCGR and FCGD. Because modelling every individual cycle in a crack growth simulation using the FE method is not feasible, a step-wise approach is often used in which the crack is extended incrementally. To be able to use a FCGD criterion in such a framework, it should be independent of the increment size. This independency is shown in Fig. 13(b) for proportional load. For non-proportional load, if the crack extension is small with respect to the initial notch and the nominal stress remains approximately constant, it is shown that for some criteria the predicted crack path is dependent on the crack increment size, but the predicted FCGD is independent on the number of crack extensions steps, meaning that the predicted FCGD after i steps is approximately constant, see Fig. 23(a). In contrast to the proportional validation case Section 3.4, the simulations shown in Section 4 all have an (approximately) constant nominal stress field throughout the crack growth, ignoring any boundary effects. Therefore, for the first few crack extension steps the same FCGD is predicted independent of the crack increment size. Based on the simulations it is shown that the MTS, HP and MPZR criteria predict a FCGD which maximizes the governing quantity in the first step. After that, the FCGD remains approximately constant. Hence, an unambiguous FCGD results for these criteria. For the VCTD, VCTD* and MSSR criteria, however, the predicted FCGD changes with each extension step. Hence, there is no unique FCGD, and an additional condition is required to define the final FCGD. Such a condition is currently lacking. In some simulations, the crack extends in such a way that a negative K_I arises during part of the cycle. In the current framework the simulation is then terminated. Expanding the simulations by including contact will alter the SIF evolution and thereby the FCGD which would enable continuing the simulation. However, defining contact in a mixed mode testing is a study on its own. Another extension would be to relate the SIFs with the FCGR. By assuming a fixed number of cycles per crack increment, for every simulation step a different crack increment is determined based on the SIF evolution. This would require a FCGR applicable to non-proportional mixed-mode load which is currently not available.

5.3. Design of experiments

Fatigue crack growth experiments are often designed to measure the FCGR instead of the FCGD. This was also the case in the experiments elaborated in this research. The sudden changes in the loading phase in Experiment I and Experiment II resulted in changes in the plasticity around the crack-tip, which are not captured by any of the used FCGD criteria. In Experiments A, B and C these changes were also present. An additional challenge in this second set of experiments is the lack of high quality photos to accurately measure the crack path. It is therefore recommended to conduct more mixed-mode fatigue crack growth experiments that also focus on FCGD.

In practice, some types of structures, for example rails and bridges, are subjected to repetitive load with approximately constant non-proportionality (i.e. constant ϕ_K) throughout the lifetime. In experiments this is not always the case, for example in Experiment I and II, see Figs. 14(b) and 20(b). Any change in load sequence will change the development of plasticity around the crack tip and therefore influence the FCGR and FCGD. This makes such tests difficult to interpret. Pre-cracking in mixed mode tests is usually done in Mode-I, hence an unavoidable change in load sequence is present. It is recommended to conduct experiments with constant non-proportionality in which the pre-crack SIF range is as small as possible, to limit this plasticity development. Additionally, to investigate the effect of plasticity, it recommended to conduct experiments with either different specimen thicknesses or with different grades (different yield and tensile strengths). Thicker specimen lead to a more plane-strain state, which results in less effect of plasticity compared to a plane stress state in thin specimens. Similarly, high-strength material develops less crack tip plasticity compared to low strength material. Finally, it is proposed to conduct series of experiments where a single loading parameter, such as the biaxiality range $\Delta\lambda$ or the load phase shift ϕ_F, is varied between the tests, to obtains its influence.

All experiments carried out on non-proportional load are unique, i.e. no repetitive experiments have been found. Hence, it is not known

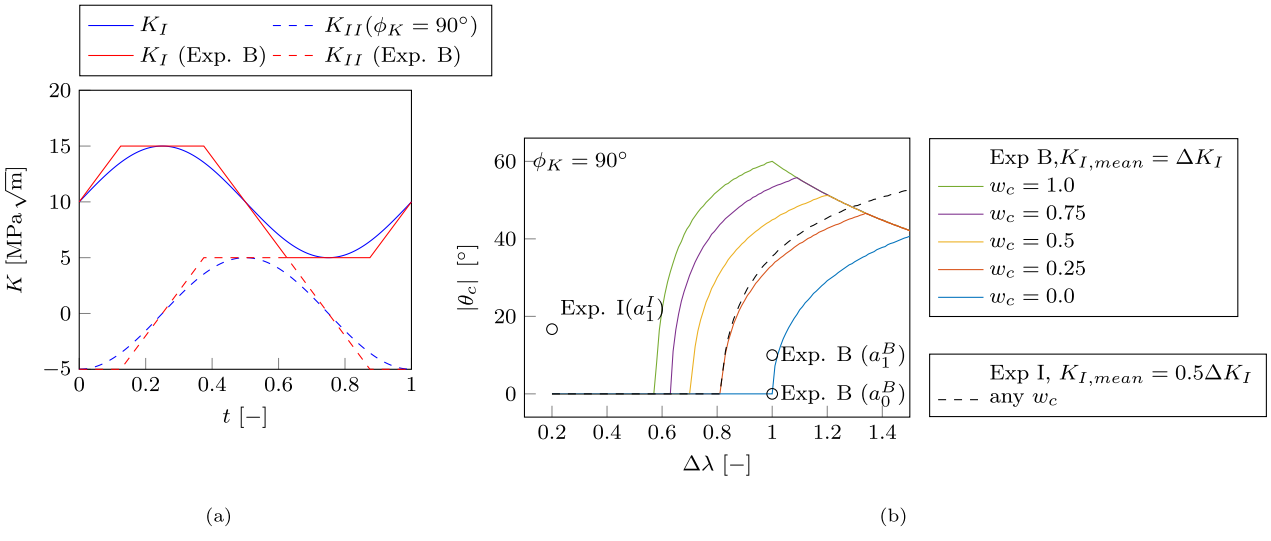

Fig. 28. (a) Idealization of Experiment B "square" as continuous (sinusoidal) signal with $\phi_K = 90°$ (b) Influence of biaxiality ratio $\Delta\lambda$ on FCGD angle using the MTS criterion.

if the crack paths and possibly branching shown in the experiments are a consistent trend or that it is a random process, e.g. related to the local microstructure. Evaluation of the crack-paths on both sides of the initial notch in a cruciform specimen could already give some indication for this. Multiple experiments carried out in the same conditions would give more insight into crack path variation.

6. Conclusions and outlook

This paper evaluates several fatigue crack growth direction (FCGD) criteria based on linear elastic fracture mechanics by comparing predicted directions with non-proportional experimental data from two literature sources [15,42]. The stress intensity factors (SIFs) of the experiments are determined using the virtual crack closure technique method, for which the finite element (FE) method is employed. The FCGD criteria are evaluated in two ways, namely, comparing them at individual instances along the experimentally obtained crack path, and comparing crack paths. An incremental crack growth scheme is used, for the latter evaluation, in which the crack path is updated with finite increments. Based on performed analyses, the following conclusions are made:

- None of the studied FCGD criteria is able to correctly predict the complete crack paths of the non-proportional experiments of study. The predicted FCGD of some criteria depend on the number of crack extension steps.
- A good estimation of the FCGD at a specific crack length does not ensure that the complete crack path is predicted correctly. A small deviation in the angle can lead to a large cumulative error when predicting the complete crack path.
- Although it is not the focus of this study, it appears that an accurate prediction of the fatigue crack growth rate for non-proportional mixed mode load is important to predict the complete crack path.
- The prediction of the FCGD at individual crack lengths depends on discretization of the crack path in the FE model.
- More experimental research for specific cases, for example non-proportional mixed-mode tests with different biaxiality ratios, could lead to additional understanding of the underlying mechanism. In these experimental programs, it is also important to do repetitive experiments quantifying the scatter in crack paths.
- The development of elastic–plastic FE models could lead to a better understanding of the interaction between the different fatigue crack growth modes. Currently, because of the lack of understanding, this elastic–plastic interaction is not included in the studied prediction models.

CRediT authorship contribution statement

Sjoerd T. Hengeveld: Writing – original draft, Visualization, Software, Methodology, Formal analysis, Conceptualization. **Davide Leonetti:** Writing – review & editing, Supervision, Funding acquisition, Conceptualization. **H.H. (Bert) Snijder:** Writing – review & editing, Supervision. **Johan Maljaars:** Writing – review & editing, Supervision, Funding acquisition, Conceptualization.

Declaration of competing interest

The authors declare that they have no known competing financial interests or personal relationships that could have appeared to influence the work reported in this paper.

Acknowledgements

This research was carried out under project number T20008 in the framework of the Research Program of the Materials innovation institute (M2i) (www.m2i.nl) supported by Holland High Tech | TKI HSTM via the PPS allowance scheme for public–private partnerships. The Dutch railway asset owner ProRail is acknowledged for its contribution to this research.

Data availability

Supplementary material including simulations files is available at https://zenodo.org/records/15807377.

References

[1] N. Perez, Fracture Mechanics, Springer International Publishing, 2017, http://dx.doi.org/10.1007/978-3-319-24999-5.
[2] A. Fatemi, N. Shamsaei, Multiaxial fatigue: An overview and some approximation models for life estimation, Int. J. Fatigue 33 (8) (2011) 948–958, http://dx.doi.org/10.1016/j.ijfatigue.2011.01.003.
[3] H. Richard, A. Eberlein, G. Kullmer, Concepts and experimental results for stable and unstable crack growth under 3D-mixed-mode-loadings, Eng. Fract. Mech. 174 (2017) 10–20, http://dx.doi.org/10.1016/j.engfracmech.2016.12.005.
[4] S.M.O. Tavares, P.M.S.T. de Castro, Equivalent stress intensity factor: The consequences of the lack of a unique definition, Appl. Sci. 13 (8) (2023) 4820, http://dx.doi.org/10.3390/app13084820.
[5] M.C. Dubourg, V. Lamacq, A predictive rolling contact fatigue crack growth model: Onset of branching, direction, and growth—role of dry and lubricated conditions on crack patterns, J. Tribol. 124 (4) (2002) 680–688, http://dx.doi.org/10.1115/1.1479698.
[6] G. Lesiuk, M. Smolnicki, R. Mech, A. Zięty, C. Fragassa, Analysis of fatigue crack growth under mixed mode (I + II) loading conditions in rail steel using CTS specimen, Eng. Fail. Anal. 109 (2020) 104354, http://dx.doi.org/10.1016/j.engfailanal.2019.104354.
[7] P. Köster, C. Benz, H. Heyer, M. Sander, In-phase and out-of-phase mixed mode loading: Investigation of fatigue crack growth in SEN specimen due to tension–compression and torsional loading, Theor. Appl. Fract. Mech. 108 (2020) 102586, http://dx.doi.org/10.1016/j.tafmec.2020.102586.
[8] J. Qian, A. Fatemi, Mixed mode fatigue crack growth: A literature survey, Eng. Fract. Mech. 55 (6) (1996) 969–990, http://dx.doi.org/10.1016/s0013-7944(96)00071-9.
[9] A.T. Yokobori, T. Yokobori, K. Sato, K. Syoji, Fatigue crack growth under mixed modes I and II, Fatigue Fract. Eng. Mater. Struct. 8 (4) (1985) 315–325, http://dx.doi.org/10.1111/j.1460-2695.1985.tb00430.x.
[10] Y. Kong, S. Abdullah, D. Schramm, M. Omar, S. Haris, Correlation of uniaxial and multiaxial fatigue models for automobile spring life assessment, Exp. Tech. 44 (2) (2019) 197–215, http://dx.doi.org/10.1007/s40799-019-00344-w.
[11] U. Zerbst, R. Lunden, K.-O. Edel, R. Smith, Introduction to the damage tolerance behaviour of railway rails a review, Eng. Fract. Mech. 76 (17) (2009) 2563–2601, http://dx.doi.org/10.1016/j.engfracmech.2009.09.003.
[12] T. Reis, A.P.C. Dias, A.A. Santos, A fast method to estimate the multiaxial non-proportional elastic–plastic stress–strain in rail rolling contact fatigue problems, Int. J. Solids Struct. 241 (2022) 111516, http://dx.doi.org/10.1016/j.ijsolstr.2022.111516.
[13] M. Duan, Y. Li, H. Liu, Y. Shu, Fatigue crack behaviors under asynchronous biaxial loading, Int. J. Fatigue 126 (China) (2019) 248–257, http://dx.doi.org/10.1016/j.ijfatigue.2019.05.006.
[14] C.H. Wolf, S. Henkel, A. Burgold, Y. Qiu, M. Kuna, H. Biermann, Fatigue crack growth in austenitic stainless steel: Effects of phase shifted loading and crack paths, Adv. Eng. Mater. 21 (5) (2018) 1800861, http://dx.doi.org/10.1002/adem.201800861.
[15] C.H. Wolf, S. Henkel, A. Burgold, Y. Qiu, M. Kuna, H. Biermann, Investigation of fatigue crack growth under in-phase loading as well as phase-shifted loading using cruciform specimens, Int. J. Fatigue 124 (2019) 595–617, http://dx.doi.org/10.1016/j.ijfatigue.2019.03.011.
[16] R. Neerukatti, S. Datta, A. Chattopadhyay, N. Iyyer, N. Phan, Fatigue crack propagation under in-phase and out-of-phase biaxial loading, Fatigue Fract. Eng. Mater. Struct. 41 (2) (2017) 387–399, http://dx.doi.org/10.1111/ffe.12690.
[17] D. Floros, A. Ekberg, F. Larsson, Evaluation of crack growth direction criteria on mixed-mode fatigue crack growth experiments, Int. J. Fatigue 129 (2019) 105075, http://dx.doi.org/10.1016/j.ijfatigue.2019.04.013.
[18] D. Infante-García, G. Qian, H. Miguélez, E. Giner, Analysis of the effect of out-of-phase biaxial fatigue loads on crack paths in cruciform specimens using XFEM, Int. J. Fatigue 123 (2019) 87–95, http://dx.doi.org/10.1016/j.ijfatigue.2019.01.019.
[19] M. Zaid, V. Bonnand, V. Doquet, V. Chiaruttini, D. Pacou, P. Depouhon, Fatigue crack growth in bearing steel under cyclic mode II + static biaxial compression, Int. J. Fatigue 163 (2022) 107074, http://dx.doi.org/10.1016/j.ijfatigue.2022.107074.
[20] P. Bold, Multiaxial Fatigue Crack Growth in Rail Steel (Ph.D. thesis), University of Sheffield, 1990.
[21] T. Bonniot, V. Doquet, S.H. Mai, Fatigue crack growth under non-proportional mixed-mode. Role of compression while shearing, Int. J. Fatigue 134 (2020) 105513, http://dx.doi.org/10.1016/j.ijfatigue.2020.105513.

[22] T. Bonniot, Fissuration par fatigue en mode mixte non proportionnel des rails de chemins de fer: De l'étude expérimentale à la mise en œuvre d'un modèle (Ph.D. thesis), (2019SACLX096) Université Paris-Saclay, 2019, URL: https://tel.archives-ouvertes.fr/tel-02443488.

[23] A. Otsuka, K. Tohgo, H. Matsuyama, Fatigue crack initiation and growth under mixed mode loading in aluminum alloys 2017-T3 and 7075-T6, Eng. Fract. Mech. 28 (5–6) (1987) 721–732, http://dx.doi.org/10.1016/0013-7944(87)90065-8.

[24] P. Zerres, M. Vormwald, Review of fatigue crack growth under non-proportional mixed-mode loading, Int. J. Fatigue 58 (2014) 75–83, http://dx.doi.org/10.1016/j.ijfatigue.2013.04.001.

[25] V. Doquet, M. Abbadi, Q.H. Bui, A. Pons, Influence of the loading path on fatigue crack growth under mixed-mode loading, Int. J. Fract. 159 (2) (2009) 219–232, http://dx.doi.org/10.1007/s10704-009-9396-6.

[26] F. Erdogan, G.C. Sih, On the crack extension in plates under plane loading and transverse shear, J. Basic Eng. 85 (4) (1963) 519–525, http://dx.doi.org/10.1115/1.3656897.

[27] G.C. Sih, Strain-energy-density factor applied to mixed mode crack problems, Int. J. Fract. 10 (3) (1974) 305–321, http://dx.doi.org/10.1007/bf00035493.

[28] K. Palaniswamy, W.G. Knauss, Propagation of a crack under general, in-plane tension, Int. J. Fract. Mech. 8 (1) (1972) 114–117, http://dx.doi.org/10.1007/bf00185207.

[29] A. Otsuka, K. Mori, T. Miyata, The condition of fatigue crack growth in mixed mode condition, Eng. Fract. Mech. 7 (3) (1975) 429–439, http://dx.doi.org/10.1016/0013-7944(75)90043-0.

[30] S. Highsmith, Crack Path Determination for Non-Proportional Mixed-Mode Fatigue (Ph.D. thesis), George W. Woodruff School of Mechanical Engineering, 2009.

[31] K. Walker, The effect of stress ratio during crack propagation and fatigue for 2024-T3 and 7075-T6 aluminum, in: Effects of Environment and Complex Load History on Fatigue Life, ASTM International, 1970, pp. 1–1–14, http://dx.doi.org/10.1520/stp32032s.

[32] D. Amato, L. Mayrhofer, C. Robl, G. Dhondt, R. Citarella, Prediction of the crack growth propagation direction in non-proportional mixed-mode missions, Int. J. Fatigue 166 (2023) 107233, http://dx.doi.org/10.1016/j.ijfatigue.2022.107233.

[33] J. Newman, A crack opening stress equation for fatigue crack growth, Int. J. Fract. 24 (4) (1984) R131–R135, http://dx.doi.org/10.1007/bf00020751.

[34] S. Mettu, V. Shivakumar, J. Beek, F. Yeh, L. Williams, R. Forman, J. McMahon, I. Newman, NASGRO 3.0: A software for analyzing aging aircraft, in: The Second Joint NASA/FAA/DoD Conference on Aging AircraftIssue: Pt. 2, 1999, pp. 792–801.

[35] S. Suresh, R.O. Ritchie, A geometric model for fatigue crack closure induced by fracture surface roughness, Met. Trans. A 13 (9) (1982) 1627–1631, http://dx.doi.org/10.1007/bf02644803.

[36] E.K. Tschegg, S.E. Stanzl, H.R. Mayer, M. Czegley, Crack face interactions and near-threshold fatigue crack growth, Fatigue Fract. Eng. Mater. Struct. 16 (the) (1992) 71–83, http://dx.doi.org/10.1111/j.1460-2695.1993.tb00071.x.

[37] X. Yu, A. Abel, Crack surface interference under cyclic mode I and steady mode II loading part I: Experimental study, Eng. Fract. Mech. 66 (6) (2000) 503–518, http://dx.doi.org/10.1016/s0013-7944(00)00038-2.

[38] X. Yu, A. Abel, Modelling of crack surface interference under cyclic shear loads, Fatigue Fract. Eng. Mater. Struct. 22 (3) (1999) 205–213, http://dx.doi.org/10.1046/j.1460-2695.1999.00152.x.

[39] N. Chen, F. Lawrence, An analytical model for studying roughness-induced crack closure, in: Fatigue and Fracture Mechanics, vol. 29, ASTM International, 1999, pp. 535–550, http://dx.doi.org/10.1520/STP14968S.

[40] J. Crapps, S. Daniewicz, A macrostructural model for simulating the combined effects of roughness and plasticity induced fatigue crack closure, Int. J. Fatigue 45 (2012) 15–30, http://dx.doi.org/10.1016/j.ijfatigue.2012.06.017.

[41] S. Pommier, Development of an incremental model for fatigue crack growth predictions, AerospaceLab J. (9) (2015) http://dx.doi.org/10.12762/2015.AL09-11, (ISSN: 2107–6596) June 2015.

[42] F. Fremy, S. Pommier, M. Poncelet, B. Raka, E. Galenne, S. Courtin, J.-C.L. Roux, Load path effect on fatigue crack propagation in I+II+III mixed mode conditions – part 1: Experimental investigations, Int. J. Fatigue 62 (2014) 104–112, http://dx.doi.org/10.1016/j.ijfatigue.2013.06.002.

[43] F. Fremy, S. Pommier, E. Galenne, S. Courtin, J.-C.L. Roux, Load path effect on fatigue crack propagation in I+II+III mixed mode conditions – part 2: Finite element analyses, Int. J. Fatigue 62 (2014) 113–118, http://dx.doi.org/10.1016/j.ijfatigue.2013.06.007.

[44] R. Hamam, S. Pommier, F. Bumbieler, Variable amplitude fatigue crack growth, experimental results and modeling, Int. J. Fatigue 29 (9–11) (2007) 1634–1646, http://dx.doi.org/10.1016/j.ijfatigue.2007.02.005.

[45] P. Dahlin, M. Olsson, The effect of plasticity on incipient mixed-mode fatigue crack growth, Fatigue Fract. Eng. Mater. Struct. 26 (7) (2003) 577–588, http://dx.doi.org/10.1046/j.1460-2695.2003.00622.x.

[46] F. Hourlier, A. Pineau, Propagation of fatigue cracks under polymodal loading, Fatigue Fract. Eng. Mater. Struct. 5 (4) (1982) 287–302, http://dx.doi.org/10.1111/j.1460-2695.1982.tb01237.x.

[47] K. Golos, B. Wasiluk, Role of plastic zone in crack growth direction criterion under mixed mode loading, Int. J. Fract. 102 (4) (2000) 341–353, http://dx.doi.org/10.1023/a:1007663728926.

[48] H. Tada, P.C. Paris, G.R. Irwin, The Stress Analysis of Cracks Handbook, third ed., ASME Press, 2000, http://dx.doi.org/10.1115/1.801535.

[49] S. Henkel, C. Wolf, H. Biermann, A. Burgold, M. Kuna, Cruciform specimens used for determination of the influence of T-stress on fatigue crack growth with overloads on aluminum alloy Al 6061 T651, Frat. Integrità Strutt. 13 (48) (2019) 135–143, http://dx.doi.org/10.3221/igf-esis.48.16.

[50] F. Fremy, Fissuration par fatigue en mode mixte I+II+III non proportionnel dans l'acier 316L : approche expérimentale et modélisation des effets de la plasticité (Ph.D. thesis), École normale supérieure de Cachan - ENS Cachan, 2013.

[51] H.A. Richard, M. Fulland, M. Sander, Theoretical crack path prediction, Fatigue Fract. Eng. Mater. Struct. 28 (1–2) (2004) 3–12, http://dx.doi.org/10.1111/j.1460-2695.2004.00855.x.

[52] C. Li, Vector CTD criterion applied to mixed mode fatigue crack growth, Fatigue Fract. Eng. Mater. Struct. 12 (1) (1989) 59–65, http://dx.doi.org/10.1111/j.1460-2695.1989.tb00508.x.

[53] Westergaard, Bearing pressure and cracks, 1939.

[54] D. Floros, A. Ekberg, F. Larsson, Evaluation of mixed-mode crack growth direction criteria under rolling contact conditions, Wear 448–449 (2020) 203184, http://dx.doi.org/10.1016/j.wear.2020.203184.

[55] Wasiluk, Golos, Prediction of crack growth direction under plane stress for mixed-mode I and II loading, Fatigue Fract. Eng. Mater. Struct. 23 (5) (2000) 381–386, http://dx.doi.org/10.1046/j.1460-2695.2000.00300.x.

[56] L. Pook, The effect of crack angle on fracture toughness, Eng. Fract. Mech. 3 (3) (1971) 205–218, http://dx.doi.org/10.1016/0013-7944(71)90032-4.

[57] DassaultSystems, Abaqus FEA, 2020.

[58] R.S. Barsoum, On the use of isoparametric finite elements in linear fracture mechanics, Internat. J. Numer. Methods Engrg. 10 (1) (1976) 25–37, http://dx.doi.org/10.1002/nme.1620100103.

[59] R.D. Henshell, K.G. Shaw, Crack tip finite elements are unnecessary, Internat. J. Numer. Methods Engrg. 9 (3) (1975) 495–507, http://dx.doi.org/10.1002/nme.1620090302.

[60] E. Rybicki, M. Kanninen, A finite element calculation of stress intensity factors by a modified crack closure integral, Eng. Fract. Mech. 9 (4) (1977) 931–938, http://dx.doi.org/10.1016/0013-7944(77)90013-3.

[61] R. Krueger, Virtual crack closure technique: History, approach, and applications, Appl. Mech. Rev. 57 (2) (2004) 109–143, http://dx.doi.org/10.1115/1.1595677.

[62] I. Raju, Calculation of strain-energy release rates with higher order and singular finite elements, Eng. Fract. Mech. 28 (3) (1987) 251–274, http://dx.doi.org/10.1016/0013-7944(87)90220-7.

[63] S.T. Hengeveld, D. Leonetti, B. Snijder, J. Maljaars, Prediction of fatigue crack paths including crack-face friction for an inclined edge crack subjected to mixed mode loading, Procedia Struct. Integr. 54 (2024) 34–43, http://dx.doi.org/10.1016/j.prostr.2024.01.053.

[64] A. Miranda, M. Meggiolaro, J. Castro, L. Martha, T. Bittencourt, Fatigue crack propagation under complex loading in arbitrary 2D geometries, in: Applications of Automation Technology in Fatigue and Fracture Testing and Analysis, vol. 4, ASTM International, 2002, pp. 120–120–26, http://dx.doi.org/10.1520/stp10608s.

[65] M.S. Nezhad, D. Floros, F. Larsson, E. Kabo, A. Ekberg, Numerical predictions of crack growth direction in a railhead under contact, bending and thermal loads, Eng. Fract. Mech. 261 (2022) 108218, http://dx.doi.org/10.1016/j.engfracmech.2021.108218.

[66] P. Paris, M. Gomez, W. Anderson, A rational theory of fatigue, Trend Eng. 13 (1961) 9–14, Cited by: 1, URL: https://www.scopus.com/inward/record.uri?eid=2-s2.0-85120384671&partnerID=40&md5=50c0794a38fa646afe002a0f8c79daf8.

[67] P.-Y. Decreuse, Fissuration en mode mixte I+II non proportionnel: approche expérimentale et modélisation de la plasticité (Ph.D. thesis), École normale supérieure de Cachan - ENS Cachan, 2010.

[68] F. Fremy, S. Pommier, E. Galenne, S. Courtin, A scaling approach to model history effects in fatigue crack growth under mixed mode I+II+III loading conditions for a 316L stainless steel, Int. J. Fatigue 42 (2012) 207–216, http://dx.doi.org/10.1016/j.ijfatigue.2011.10.013.

[69] C. Packiaraj, S. Ray, S. Mannan, The influence of crack closure on the positive load ratio dependence of fatigue threshold stress intensity factor range of AISI 316 stainless steel in air at room temperature, Int. J. Press. Vessels Pip. 57 (1) (1994) 65–70, http://dx.doi.org/10.1016/0308-0161(94)90098-1.

[70] M.-L. Zhu, F.-Z. Xuan, S.-T. Tu, Interpreting load ratio dependence of near-threshold fatigue crack growth by a new crack closure model, Int. J. Press. Vessels Pip. 110 (2013) 9–13, http://dx.doi.org/10.1016/j.ijpvp.2013.04.015.